Combining asynchronous microphone array measurements for enhanced acoustic imaging and volumetric source mapping

Lima Pereira, Lourenço Tércio; Merino-Martínez, Roberto; Ragni, Daniele; Gómez-Ariza, David; Snellen, Mirjam

DOI
10.1016/j.apacoust.2021.108247

Publication date
2021

Document Version
Final published version

Published in
Applied Acoustics

Applied Acoustics 182 (2021) 108247

Contents lists available at ScienceDirect

Applied Acoustics

journal homepage: www.elsevier.com/locate/apacoust

Combining asynchronous microphone array measurements for enhanced acoustic imaging and volumetric source mapping

Lourenço Tércio Lima Pereira [a,1,*], Roberto Merino-Martínez [a,*,1], Daniele Ragni [a], David Gómez-Ariza [b], Mirjam Snellen [a]

[a] Faculty of Aerospace Engineering, Delft University of Technology, Kluyverweg 1, 2629 HS Delft, The Netherlands
[b] Aerodynamics and Aeroacoustics, Parrot S.A., Quai de Jemmapes 174, 75010 Paris, France

ARTICLE INFO

Article history:
Received 12 January 2021
Received in revised form 21 May 2021
Accepted 10 June 2021

2010 MSC:
00-01
99-00

Keywords:
Acoustic imaging
Microphone arrays
Aeroacoustics
3D source mapping
Drone noise

ABSTRACT

This paper explores the advantages of combining asynchronous microphone array measurements for acoustic source mapping in two and three–dimensional applications. Four different approaches are considered, three consisting of the combination of the source maps (arithmetic mean, geometric mean, and minimum value), and a fourth one obtained by combining the cross–spectral matrices of all the asynchronous measurements into a larger matrix and applying beamforming with it. Both synthetic and experimental test cases convey enhanced results concerning the single measurement baseline, especially by reducing the spurious sidelobes. Two aeroacoustic experiments are considered, the first features a distributed sound source over a flat plate model tested in a wind tunnel and the second features a hovering drone with multiple sound sources, representing typical challenges for 2D and 3D source localization, respectively. For the 2D source mapping configuration, the sidelobe level was reduced up to 5 dB with respect to the baseline, while maintaining a similar beamwidth of the main lobe. For the 3D test cases, the approaches enable volumetric source mapping capabilities, even when planar microphone arrays are considered, commonly available in typical test facilities. Overall, the minimum value approach presents the best performance for all cases in terms of reduced main lobe beamwidth and sidelobe levels.

1. Introduction

Noise emissions are considered as one of the main environmental health threats nowadays [1] and have been assessed as an important aspect in the design of several systems, such as aircraft [2–4], wind turbines [5,6], ground vehicles [7–9], and rotating machinery [10–12]. Noise exposure on communities is limited by strict environmental laws [13]. Nevertheless, such systems typically encompass complicated distributions of multiple noise sources and, to study and mitigate the noise levels emitted, it is of paramount importance to accurately determine the location and strength of the individual noise sources [14].

Phased microphone arrays, together with acoustic imaging algorithms [15–17], have become a standard approach for sound source localization. The conventional beamforming algorithm [18,19] compares the relative phase delays between each of the microphones of the array with the delays expected from the source locations mapped (usually within a discretized scan grid). The result of this comparison is maximum when a focal position coincides with the location of the actual sound source and smaller elsewhere [19]. This process is in essence a spatial filtering that is normally performed in the frequency domain, which justifies the nomenclature conventional frequency domain beamforming (CFDBF) algorithm [15,18].

However, the limited number of microphones N available in the array (usually due to practical or budgetary reasons), restricts the array capabilities and design. Therefore, the results provided by CFDBF (and, in general, other acoustic imaging algorithms) typically suffer from limitations [20], such as:

i- A restricted spatial resolution, which hinders the proper identification and separation of sound sources closely located, especially at low frequencies. The spatial resolution is a function of the array aperture D, the evaluated sound frequency f, the speed of sound c, and the distance between the array and the sound source h. A common metror evaluating the spatial resolution

* Corresponding authors.
E-mail addresses: L.T.LimaPereira@tudelft.nl (L.T. Lima Pereira), r.merinomartinez@tudelft.nl (R. Merino-Martínez).
[1] shared first authorship

https://doi.org/10.1016/j.apacoust.2021.108247
0003-682X/

is the beamwidth (BW) of the main lobe 3 dB below its peak value. This is evaluated from the Point Spread Function (PSF) [14,21], i.e. the array response to a unitary–strength point source, and is determined by the Rayleigh resolution limit [22], being roughly estimated as BW $\approx 1.22ch/(Df)$. Therefore, larger values of D and f and smaller values of h generally provide a better spatial resolution;

ii- The presence of sidelobes or spurious sources which could be misinterpreted as real sources. These sidelobes are a consequence of the finite size and microphone density of the array. As such, they can be considered as the diffraction pattern of the phased array [21] representing regions where spurious noise from a dominant source has a constructive sum causing a local maximum region in the source map. The number of microphones N and their distribution within the array are the main parameters influencing the sidelobe level (SL). A common metric for evaluating the presence of sidelobes is the maximum sidelobe level (MSL), which is determined as the difference (in decibels) between the highest sidelobe and the main lobe's peak. With this criterion, the MSL has values smaller or equal to zero. Besides, to avoid spatial aliasing (and the so–called grating lobes [21]), the spacing between microphones should be small with respect to the wavelength to be resolved (e.g. smaller than half the wavelength of the sound of interest for linear arrays).

Therefore, a compromise solution is usually sought for achieving acceptable BW (requiring arrays with large aperture) and SL (requiring densely populated arrays) values. For a given value of N, different optimization approaches [23–26] can be employed to improve the response of the array results.

Moreover, the limited value of N led to a predominant use of linear and especially planar microphone arrays [15], partly due to their simplicity in terms of design and setup, but also because of the typical use of planar scan grids parallel to the array plane which contain the expected locations of the sound sources of interest. Even if beamforming can be applied in a three–dimensional domain, the spatial resolution in the normal direction to the array plane (i.e. depthwise) is usually poor [27,28] and can only be marginally improved by the application of microphone weighting schemes [29]. Therefore, the separation of sound sources in the array plane's normal direction is particularly difficult [30]. Nevertheless, three–dimensional (3D) acoustic source mapping is gaining interest lately for the study of complex sound source arrangements, such as aircraft components [31–34], airfoils [28,35] and passenger vehicles [30,36,37]. This application requires a considerably larger computational time due to the higher number of grid points and an adapted formulation of the acoustic imaging algorithm [29,35,38–42].

A straightforward manner to further improve the BW and SL values of the acoustic source maps is to increase the number of microphone channels N. However, the associated cost is usually a limitation within the design of a new acoustic array. For the case of volumetric source mapping, the use of three–dimensional microphone arrays [28,43–45] or the synchronous use of several planar microphone arrays placed in different planes [33,40,42,46] is preferred for palliating the aforementioned effect of the poor depth resolution of planar arrays. However, this approach leads to a dedicated experimental setup, which also implies a large value of N and a specific arrangement for the microphone positions.

An alternative approach to additionally enhance the acoustic source maps is to virtually increase N by combining the results of multiple asynchronous microphone array measurements, in which the sound source remains at the same location but the microphone array is displaced to different positions to obtain different points of view [47–52]. In this way, higher spatial sampling is obtained. The sound field needs to be stationary, i.e. the sound emissions should not vary with time [53]. This approach benefits from the fact that the sidelobe pattern of the array (i.e. the PSF) is strongly dependent on the relative location between the sound source and the microphone array. Therefore, measurements using different array locations will present different sidelobe patterns, which can be exploited to further improve the quality of the source maps. This concept is further explained in Section 2. A comparable procedure can be employed when averaging source maps in the frequency domain since the sidelobe pattern is also frequency–dependent [54].

This paper investigates the use of multiple asynchronous measurements with a planar array (normally called prototype array) placed at different positions for improving the standard results obtained with a single measurement, both in two– and three–dimensional source mapping applications. A motivation for this research is that a large number of experimental facilities, such as aeroacoustic wind tunnels [36,55–63], are equipped with (at least) a single planar microphone array that can be easily displaced within the measurement room and could benefit from this approach. In this study, the microphone distribution of the prototype microphone array is kept constant to reduce the operational time required.

It should be noted that the use of advanced deconvolution or inverse acoustic imaging methods [58,64–66] can also enhance the quality of the standard CFDBF source maps. The use of advanced methods (such as DAMAS [67]) for volumetric source mapping applications, however, can become prohibitive due to the computational demand of the larger number of grid points and microphone positions. These methods are not considered in this paper for the sake of brevity, but, since most of them are based on CFDBF, a potential improvement in the CFDBF results is also expected to be reflected in the outcome of more advanced techniques [25,33].

The approaches considered for combining the multiple asynchronous measurements are explained in Section 2. These techniques are applied first to experimental measurements featuring an omnidirectional speaker at the anechoic, vertical, open–jet wind tunnel (A–tunnel) of Delft University of Technology. Synthetic cases replicating the source arrangements in the experiments are also evaluated. In addition, more complex experiments featuring a flat plate tested in the A–tunnel, as well as a hovering drone, are also analyzed. The simulated and experimental setups employed are described in Section 3. The results obtained are discussed in Section 4 for both the 2D and 3D applications. Lastly, the conclusions are drawn in Section 5.

2. Methodology

2.1. Conventional Frequency Domain Beamforming (CFDBF)

CFDBF is the most common method for source mapping, since it is robust, fast, and intuitive [18]. This technique considers the recorded pressure history in each of the N microphones of the array in the frequency domain as an N–dimensional vector $\boldsymbol{p}(f) \in \mathbb{C}^{N\times 1}$, with frequency (f) dependence

$$\boldsymbol{p}(f) = \begin{pmatrix} p_1(f) \\ \vdots \\ p_N(f) \end{pmatrix}. \tag{1}$$

Considering a single sound source at the scan point ξ_j, the received signal is modeled as $s_j \boldsymbol{g}_j$, where s_j is the source strength and

$\boldsymbol{g}_j \in \mathbb{C}^{N\times 1}$ is the so–called steering vector. The steering vector has N components, $g_{j,n}$, $n \in [1 \dots N]$, and represents the modeled acoustic transfer function between the pressure amplitudes at the mapped source location and at the microphone locations [15]. Several steering vector formulations are available in the literature [39]. Specific radiation patterns [40,68] and the effect of a moving sound source or a moving medium (like in a wind tunnel) can be accounted for in the steering vector formulation [69]. For simplicity, omnidirectional, uncorrelated monopole sources are normally considered and differences between formulations are given by the normalization of the steering vectors. For a stationary point source, the steering vector is the free–field Green's function related to Helmholtz's equation [15]

$$g_{j,n} = \frac{\exp\left(-2\pi i f \Delta t_{j,n}\right)}{4\pi|\boldsymbol{x}_n - \xi_j|} = \frac{\exp\left(\frac{-2\pi i f|\boldsymbol{x}_n - \xi_j|}{c}\right)}{4\pi|\boldsymbol{x}_n - \xi_j|}, \tag{2}$$

where $|\cdot|$ is the Euclidean norm of the vector, $i^2 = -1$, $\Delta t_{j,n}$ is the time delay between the emission and the reception of the signal by the observer and $\boldsymbol{x}_n = (x_n, y_n, z_n) \in \mathbb{R}^{N\times 3}$, $n = 1 \dots N$ are the locations of the N microphones.

An estimate for the source autopower, A, at a (potential) sound source located at grid point ξ_j is obtained by minimizing (in a least–squares sense) the difference between the recorded pressure vector, $\boldsymbol{p}$, and the modeled pressures for a source at that grid point $\xi_j, s_j\boldsymbol{g}_j$

$$A(\xi_j) = \frac{\boldsymbol{g}_j^* \langle \boldsymbol{p}\boldsymbol{p}^* \rangle \boldsymbol{g}_j}{|\boldsymbol{g}_j|^4}. \tag{3}$$

In Eq. (3) the operator $(\cdot)^*$, denotes the complex conjugate transpose of a vector and $\langle\cdot\rangle$ denotes the time average of several snapshots. For three–dimensional applications, it is recommended to change the exponent in the denominator to a value of two instead of four [39,70] to obtain more accurate source location results. The term $\boldsymbol{C}$ is the $N \times N$ cross–spectral matrix (CSM) of the measured acoustic pressures, generated by averaging the Fourier–transformed sample blocks over time

$$\boldsymbol{C} = \langle \boldsymbol{p}\boldsymbol{p}^* \rangle. \tag{4}$$

The CSM contains the phase shifts between all combinations of microphone pairs among the array and brings the requirement for synchronous measurements within the microphone array as this is the foundation of the algorithm.

A CFDBF source map can be constructed by applying Eq. (3) to the J points defining the selected scan grid.

The combination of multiple asynchronous measurements can be used to improve the quality of the obtained source map [52]. Besides, the limited performance of a planar array for 3D source localization can be significantly enhanced by combining measurements from different views using the same array. The methods explained henceforth consider a combination of N_s microphone array measurements using CFDBF, in which the array is placed at different locations. It should be noted that the main diagonal of the CSM [65] was not removed in any of the results presented in this manuscript.

2.2. Arithmetic mean

The first method consists on simply performing the arithmetic mean of the N_s CFDBF source maps obtained from different array positions [50,71]:

$$A_{\text{arithmetic}}(\xi_j, f) = \frac{1}{N_s}\sum_{i=1}^{N_s} A_i(\xi_j, f). \tag{5}$$

This approach was applied by Castellini and Sassaroli [71] to sound sources in a reverberant environment to reduce the influence of mirror sources, i.e. not sidelobes but acoustic reflections.

2.3. Geometric mean

A similar technique uses the geometric mean of the N_s source maps [50] (i.e. multiplication instead of summation):

$$A_{\text{geometric}}(\xi_j, f) = \sqrt[N_s]{\prod_{i=1}^{N_s} A_i(\xi_j, f)}. \tag{6}$$

A three–dimensional application of this multiplicative approach was also employed by Porteous et al. [40] when using two planar microphone arrays orthogonal to each other. In their study, they also considered the deconvolution method CLEAN–SC [52,72] and dipole sources. This approach was also recently used with the enhanced high–resolution version of CLEAN–SC (EHR–CLEAN–SC [25]) in wind–tunnel experiments featuring a landing gear model and three planar arrays located in different planes [34].

2.4. Minimum value

The third method considers, for each scan point ξ_j and frequency f, the minimum value within the source autopowers ($A_i(\xi_j, f)$, with $i = 1 \dots N_s$) of all the asynchronous measurements.

$$A_{\text{minimum}}(\xi_j, f) = \min\left[A_i(\xi_j, f)\right]. \tag{7}$$

This approach was suggested and applied to numerical data by Evans et al. [30].

2.5. Combined CSM

The last approach considered employs a *combined* CSM ($\boldsymbol{C}_{\text{combined}}$) that consists of the CSMs of each of the N_s asynchronous measurements, i.e. the number of microphones is virtually increased N_s times. The CSMs of the N_s measurements are arranged in block diagonal positions and the remaining positions (i.e. the cross–correlations between pairs of microphones from different measurements) are padded by zero elements. In this way, the $(NN_s) \times (NN_s)$ matrix $\boldsymbol{C}_{\text{combined}}$ is defined as:

$$\boldsymbol{C}_{\text{combined}} = \begin{pmatrix} \boldsymbol{C}_1 & \boldsymbol{0} & \boldsymbol{0} \\ \boldsymbol{0} & \ddots & \boldsymbol{0} \\ \boldsymbol{0} & \boldsymbol{0} & \boldsymbol{C}_{N_s} \end{pmatrix}, \tag{8}$$

where $\boldsymbol{C}_i, i \in [1 \dots N_s]$ is the $N \times N$ CSM of the i^{th} asynchronous measurement defined with Eq. (4) and $\boldsymbol{0}$ is a $N \times N$ matrix filled of zeros.

This zero–padding poses a loss of information that synchronous measurements would not suffer. Some studies [51–53] have investigated the possibility of reconstructing the missing elements within $\boldsymbol{C}_{\text{combined}}$, but such processes are cumbersome and require several assumptions about the characteristics of the sound sources (such as the number of sources, their sparsity [51], and the signal to noise ratio [53]) present in the experiment [51,52]. Due to their complexity, these CSM reconstruction attempts are, therefore, not considered in this manuscript.

Substituting Eq. (8) into Eq. (3) provides

$$A_{\text{combined}}(\xi_j, f) = N_s \frac{\boldsymbol{g}_{j,\text{combined}}^* \boldsymbol{C}_{\text{combined}} \boldsymbol{g}_{j,\text{combined}}}{|\boldsymbol{g}_{j,\text{combined}}|^4}, \tag{9}$$

where the right hand side of the equation is now multiplied by N_s to correct for the forced presence of the $\boldsymbol{0}$ elements in the combined CSM and to obtain the correct autopower values, and $\boldsymbol{g}_{j,\text{combined}}$ is

the $(NN_s) \times 1$ combined steering vector, composed of the steering vectors (see Eq. (2)) of each asynchronous measurement considered (considering the different microphone positions), placed in a single column:

$$\boldsymbol{g}_{j,\text{combined}} = \begin{pmatrix} \boldsymbol{g}_{j,1} \\ \vdots \\ \boldsymbol{g}_{j,N_s} \end{pmatrix}. \tag{10}$$

Depending on the choice of the steering vector, this approach is essentially not different from the arithmetic mean (Section 2.2), with the exception that other post–processing techniques, e.g. CLEAN–SC [72], functional beamforming [73], etc. can be applied on the combined microphone data.

3. Experimental and synthetic setups

3.1. Synthetic test cases

Complementary simulated cases employing synthetic data were analyzed to compare with the results obtained for the experimental case featuring an omnidirectional sound source (*Experimental case I*, see Section 3.2). These simulated cases aim at recreating the same sound source distribution and setup as in the experiments. Moreover, these tests can also be used to simulate extended conditions that are not easily achievable with the current experimental setup, such as increasing the number of microphones several times.

For all synthetic cases, a virtual microphone array consisting of 64 microphones modeled as ideal transducers (i.e. no introduction of amplitude or phase distortions) was employed. The microphone distribution employed, mimics the one used for the experimental cases (see Section 3.2), i.e. an optimized multi–arm spiral arrangement [25], with 7 spiral arms of 9 microphones each, and an additional microphone located at the center of the array, that was scaled to half its original size in the x direction, with approximate dimensions of 1 m $\times$ 2 m, see Fig. 1a.

For all simulations a sampling frequency of 51.2 kHz and 30 s of recording time were employed, as it was done in the experiments. The acoustic data were averaged in time blocks of 8192 samples (giving a time block duration of 163.84 ms) and windowed using a Hanning weighting function with 50% data overlap, following Welch's method [74]. One–third–octave frequency bands are used in the paper for comparison purposes. The frequency range of interest extended from 800 Hz to 10 kHz.

For the 2D test cases, a square scan grid ranging from $x = -1$ m to $x = 1$ m and $y = -1$ m to $y = 1$ m was used (see coordinate system in Fig. 1c), with a spacing between scan points of 10 mm (i.e. 40,401 scan points). For the 3D cases, a cubic scan grid ranging from $x = -1$ m to $x = 1$ m, $y = -1$ m to $y = 1$ m, and $z = -1$ m to $z = 1$ m was used, with the same spacing between scan points (i.e. 8,120,601 scan points).

The following simulated cases were considered:

3.1.1. Synthetic case I: Single omnidirectional source in 2D

The same microphone distribution and sound source arrangement as in the 2D test of the *Experimental case I* were simulated. An omnidirectional sound source was placed at $(x, y, z) = (0, 0, 0)$ m, 1 m away from the array plane and aligned with the center microphone of the array, see Fig. 1c.

Four additional measurements were taken after virtually translating the microphone array ± 150 mm and ± 300 mm in the horizontal (y) direction with respect to the reference starting centered position, see circle markers in Fig. 1a. These array locations correspond to angular positions of the sound source of $\pm 8.53^\circ$ and $\pm 16.7^\circ$, respectively, from the normal direction of the prototype array plane at the center microphone. Furthermore, an additional test considering an array composed by the microphones of the prototype array and these four translations simultaneously, i.e. with 320 virtual microphones, was studied for comparison, see Fig. 1b. This larger array is just considered for comparison purposes, since optimizing the distribution of these 320 virtual microphones could improve the results obtained [24,25], but it was deemed out of the scope of this manuscript.

Fig. 1c also depicts the coordinate system employed throughout this paper, which is centered in the omnidirectional source position, and has its x axis in the downstream direction (i.e. vertical direction), its y axis in the horizontal direction of the prototype array plane pointing right, and its z axis in the direction normal to prototype array plane (pointing towards the array).

3.1.2. Synthetic case II: Two omnidirectional sources in 2D

Exactly the same simulated setup as in the *Synthetic case I* was used, but this time with an additional secondary sound source located at $(x, y, z) = (-0.75, 0.75, 0)$ m, i.e. at an angle of about 30° from the direction normal to the array plane and located in the same plane as the first source, see Fig. 1a. The secondary source had a sound pressure level (L_p) 12 dB lower than the first sound source. The location and level for the secondary source were selected because there is a relatively high sidelobe at that position in the PSF of the array, see Fig. 5a. In this way, the secondary source would be *hidden* under that sidelobe and difficult to detect.

3.1.3. Synthetic case III: Single omnidirectional source in 3D

In order to evaluate the volumetric acoustic source mapping performance of the methods considered, the configuration of *Synthetic case I* and *Experimental case I* was extended by rotating the array 90° in the clockwise direction, using the sound source position as a vertical axis of rotation, see Fig. 1c.

Additional comparisons were also made with respect to a synthetic cylindrical random array of 64 microphones with a radius equal to the distance from the source of the baseline array plane (1 m). Moreover, the synchronous cases when the array is rotated to different additional planes are also evaluated and compared in the separated appendix (see Appendix A).

3.2. Experimental test cases

All experiments were performed in the anechoic vertical open–jet wind tunnel (A–tunnel) at Delft University of Technology [62], composed by an anechoic plenum composed of *Flamex Basic* acoustic absorbing foam [76] wedges, resulting in a cut–off frequency of 200 Hz (i.e., free–field sound propagation conditions apply for higher frequencies). The A–tunnel has a contraction ratio of approximately 15 : 1 when equipped with a rectangular test section of 0.4 m $\times$ 0.7 m, resulting in a maximum flow velocity of 40 m/s.

An acoustic array installed in the anechoic plenum and consisting of 64 *G.R.A.S. 40PH* analog free–field microphones [77] with integrated constant current power amplifiers was employed for all the experiments. The transducers provide a flat frequency response within ± 1 dB from 50 Hz to 5 kHz and within ± 2 dB from 5 to 20 kHz. The data acquisition system (DAS) consisted of 4 *National Instruments* (NI) *PXIe–4499* sound and vibration modules with 24 bits resolution and 204.8 kHz maximum sampling rate. The boards are controlled by a computer via a NI *PXIe–8370* board. Each microphone is connected to the DAS by a 10–m long *G.R.A.S. AA0028* SMB–BNC coaxial cable [78]. The array was calibrated following the guidelines by Mueller [14], using a *G.R.A.S. 42AA* pistonphone (250 Hz, 114 dB reference) [79].

The array support structure consists of two steel perforated plates with 10 mm × 10 mm square holes in a regular grid pattern that tightly fit the microphones. Each plate is 1 m × 2 m and has a total of 8450 perforations, i.e. possible microphone positions. This design offers a compromise solution between reduced acoustic reflections (with an open area ratio of approximately 51%), robustness, and a large number of potential microphone distributions [62]. The whole structure of the array can be easily moved within the anechoic plenum of the A–tunnel, in case different angles of emission are to be measured.

The microphone distribution employed was the same as for the synthetic cases, see Fig. 1a. The aforementioned scaling in the x direction of the array was performed to ensure a clear sound propagation path when testing models in the wind tunnel that require support side plates (such as airfoils), i.e. to reduce the blocked directivity caused by the side plates [66].

For all measurements, the same signal processing parameters and scan grids as in the simulations were employed.

Three different experimental test cases were considered:

3.2.1. Experimental case I: Omnidirectional sound source

This experimental test case has essentially the same configuration as the *Synthetic cases I* and *III*. The sound source has an oblong shape with a length of 110 mm and a diameter of 20 mm, see Fig. 1d, and was custom–made by *Qsources* [80]. The source is omnidirectional in the azimuthal plane and has a flat frequency response from approximately 800 Hz to 6.3 kHz when driven by

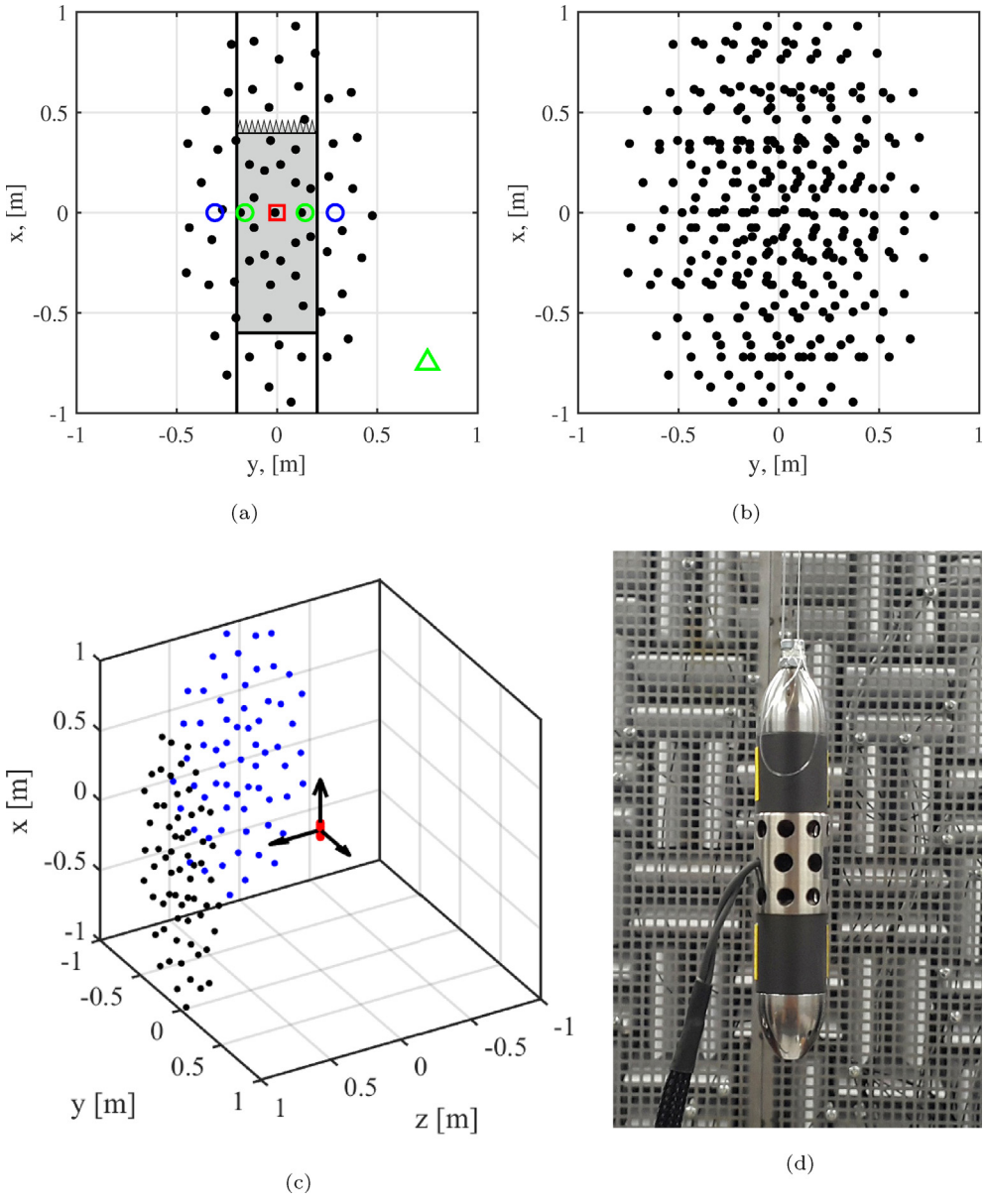

Fig. 1. (a) Microphone distribution of the prototype array denoted by the black dots. The center microphone of the arrays displaced ±0.15 m and ±0.3 m in the y direction are shown as green and blue circles, respectively. The gray rectangle shows the relative position of the flat plate whereas the vertical solid black lines denote the side plates. The □ symbol denotes the location of the omnidirectional source and the drone. The △ symbol shows the position of the secondary synthetic sound source. The flow goes in the positive x direction. (b) Virtual array with $N = 320$ obtained by displacing the prototype array ±0.15 m and ±0.3 m in the y direction. (c) Three–dimensional view of the omnidirectional sound source (red dot), the prototype array (black dots), and the array rotated 90° (blue dots). The coordinate system centered at the omnidirectional sound source is also depicted. (d) Omnidirectional sound source [75].

white noise. Therefore, in that frequency range and for this setup, this sound source is expected to perform similarly to the *Synthetic cases I* and *III*, i.e. as a quasi–monopole source. The source was placed at the center of the anechoic chamber (i.e. at $(x, y, z) = (0, 0, 0)$ m), 1 m away from the array plane and aligned with the center microphone of the array, see Fig. 1c, like in the simulated cases.

The microphone array was then moved to the same positions as in the *Synthetic case I*, i.e. ±150 mm and ±300 mm in the horizontal (y) direction with respect to the reference starting centered position, see Fig. 1a. Similarly as in the *Synthetic case III*, the microphone array was rotated 90° in the clockwise direction, using the sound source position as a vertical axis of rotation, see Fig. 1c.

All the measurements regarding the omnidirectional sound source were performed without flow in the wind tunnel, i.e. simply using the facility as an anechoic chamber.

3.2.2. Experimental case II: Flat plate interacting with the flow

In order to evaluate a more realistic experimental test case involving a distributed sound source, a flat plate model of 0.4 m span and 1 m chord was tested in the A–tunnel. The model was supported by side plates of 1.25 m length, see Fig. 2a. The plate was located at a 1 m distance from the array plane and manufactured in *plexiglass* and had a thickness of 20 mm. The elliptical leading edge was placed at $x = -0.6$ m. Three rows of staggered *LEGO*® blocks were used to increase turbulence in the incoming flow to simulate linearly–distributed uncorrelated sound sources, and to force the transition of the flow to the turbulent regime [81], see Fig. 2b. The trailing edge was located at $x = 0.4$ m and was equipped with flow–aligned sawtooth trailing–edge serrations [82]. The serrations had a height of 60 mm and a wavelength of 30 mm.

The measurements were performed at zero pressure gradient conditions and with a flow velocity of 20 m/s, which results in approximate Mach and chord–based Reynolds numbers of 0.058 and 1.35×10^6, respectively. In these conditions, the leading edge is expected to be the main noise source as a spanwise distributed sound source.

Two additional measurements were performed after displacing the microphone array ±150 mm in the horizontal (y) direction with respect to the reference centered position (prototype array).

3.2.3. Experimental case III: Hovering drone

The last experimental case consists of a hovering quadcopter drone, which represents a more complex sound source arrangement with multiple out–of–plane sources. The sources are a combination of broadband and tonal noise. The former is caused by the turbulent interaction with the blade while the latter is observed at the blade passing frequency (BPF) of the propellers and at the harmonics, i.e., multiples of the BPF. A quadcopter drone model *Parrot ANAFI* [83] in hovering mode was employed. The dimensions of the drone are 175 mm × 240 mm × 65 mm and its weight 320 g, see Fig. 3a. It is propelled by four two–bladed rotors of 60 mm of radius. It is expected to be able to operate with winds of up to 14 m/s while being relatively quiet.

The drone was placed 1 m away from the array plane, aligned with the center microphone, see Fig. 3b. The noise emissions of the drone were recorded in four measurements in which the drone was rotated 90° along the x axis with respect to each other, while the microphone array remained in the same position. During these measurements, there was no flow inside of the wind tunnel to allow for a more accurate positioning and stationary sound emissions.

The recordings had an average signal to noise ratio of 26 dB with respect to the background noise. The operational conditions tested correspond to a BPF of 350 Hz, i.e. a propeller rotational speed of 10,500 rpm [84]. Drones of this size are also expected to have a relatively strong high–frequency noise content.

4. Results and discussion

The results presented here are divided into 2D source mapping (Section 4.1) and 3D source mapping (Section 4.2). Both categories include synthetic and experimental cases. Moreover, an investigation of the influence of the number of asynchronous measurements (N_s) on the results is provided in Appendix A.

In all cases, the beamwidth (BW) of the main lobe 3 dB below the peak value and the maximum sidelobe level (MSL) are

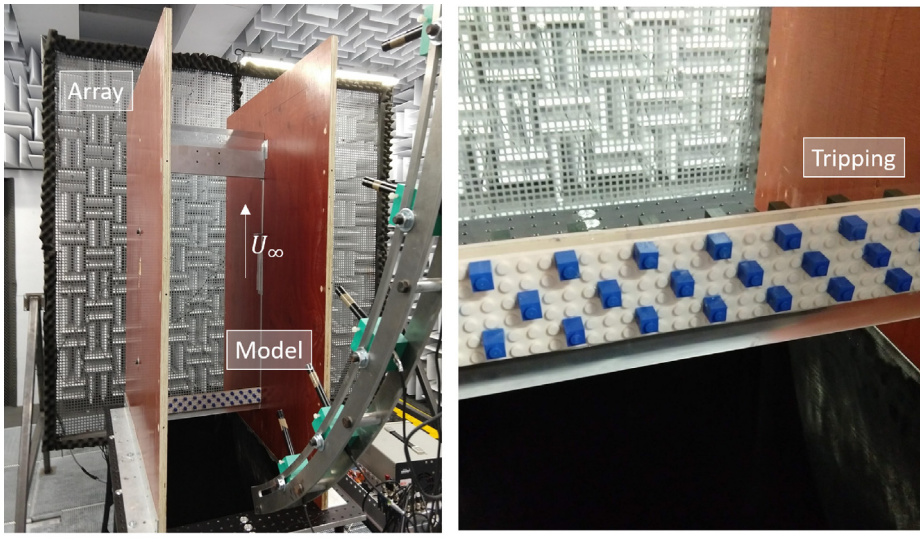

Fig. 2. (a) Experimental setup with the flat plate installed in the A–tunnel. (b) Detail of the boundary layer tripping device.

(a) (b)

Fig. 3. (a) *Parrot ANAFI* quadcopter drone [83]. (b) Drone hovering in front of the array.

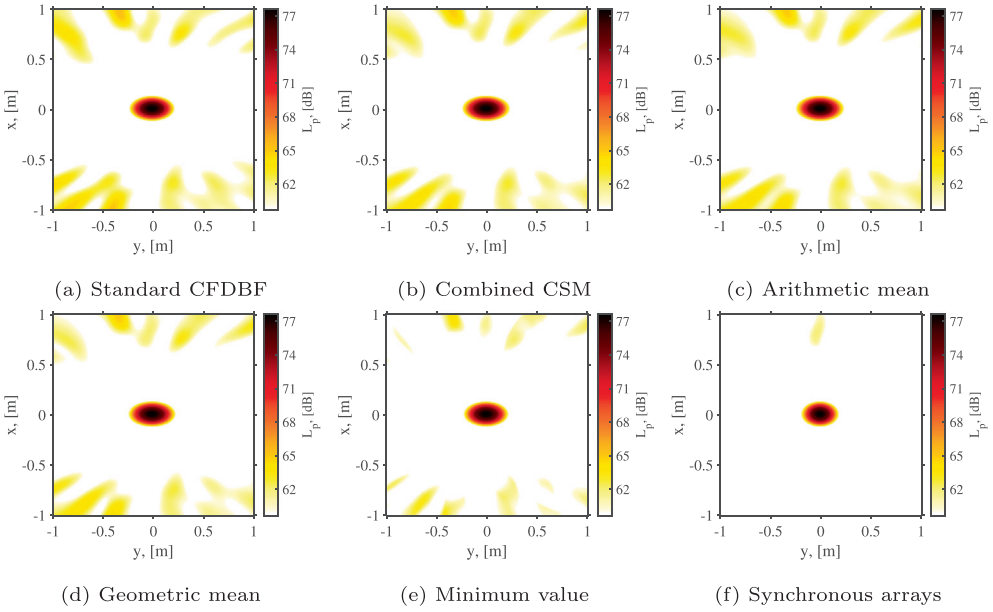

Fig. 4. Source maps for the *Synthetic case I* for the 2 kHz one–third–octave band. (a) Standard CFDBF, (b) Combined CSM, (c) Arithmetic mean, (d) Geometric mean, (e) Minimum value, (f) Synchronous arrays ($N = 320$). All the combination methods had $N_s = 5$.

evaluated. Because of the elongated shape of the prototype microphone array, the main lobe of the PSF is not axisymmetric, but rather elongated in the direction of the shortest dimension of the array (i.e. the y axis). Fig. 4a exemplifies the characteristic PSF obtained from this array geometry. For 2D source mapping, it was decided to determine the BW as the diameter ($2R$) of the equivalent circle with the same area (πR^2) as the area 3 dB below the peak of the main lobe. Conversely, for volumetric source mapping, the BW was approximated as the diameter of the equivalent sphere with the same volume ($4\pi R^3/3$) as the volume contained 3 dB below the peak of the main lobe [28]. The MSL was simply calculated as the difference (in decibels) between the highest sidelobe within the scan grid and the peak value of the main lobe, see Section 3. Additionally, the average sidelobe level is also evaluated. This metric is calculated as the mean sidelobe level (in decibels, with respect to the main lobe's peak value) outside of the main lobe within the scan grid defined. Both the maximum and the average sidelobe levels are defined as a difference with respect to the peak of the main lobe and, as such, they are less than or equal to zero [25]. With this criterion, it is desired to minimize the values of both MSL and average SL to obtain cleaner source maps.

4.1. 2D source mapping

4.1.1. Synthetic cases

An illustration of the acoustic source maps obtained from the *Synthetic case I* is depicted in Figs. 4 and 5 for one–third–octave bands centered at 2 kHz and 4 kHz, respectively.

For the 2 kHz case, the source map obtained by the standard CFDBF (i.e. $N_s = 1$, Fig. 4a) is only slightly improved by the combined CSM (Fig. 4b), arithmetic mean (Fig. 4c) and geometric mean (Fig. 4d) approaches. These three methods provide a similar sidelobe reduction with respect to the baseline case, which is better observed by the lower intensity of the highest sidelobes at $x = \pm 1$ m and $y \approx -0.4$ m. A noticeable improvement is obtained by the minimum value approach (Fig. 4e), which suppresses sev-

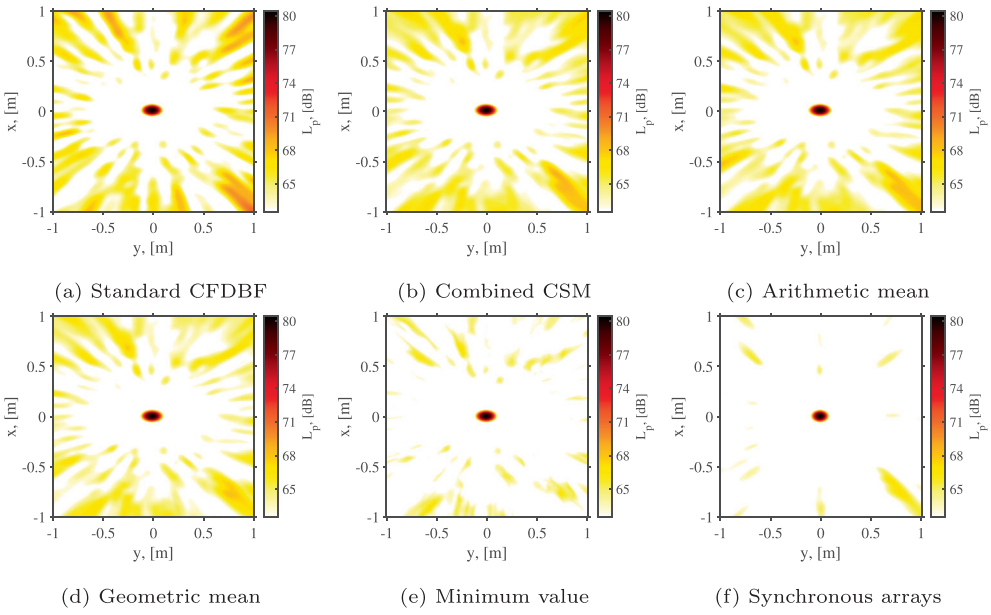

Fig. 5. Source maps for the *Synthetic case I* for the 4 kHz one–third–octave band. (a) Standard CFDBF, (b) Combined CSM, (c) Arithmetic mean, (d) Geometric mean, (e) Minimum value, (f) Synchronous arrays ($N = 320$). All the combination methods had $N_s = 5$.

eral sidelobes below the 15 dB dynamic range shown and offers the closest performance in comparison to the case with five synchronous arrays (i.e. 320 microphones, see Fig. 4f).

The 4 kHz one–third–octave band maps (Fig. 5) better reveal the differences between the approaches tested. In comparison with the standard CFDBF (Fig. 5a), improvements are achieved (in increasing order of magnitude) by the combined CSM (Fig. 5b), arithmetic mean (Fig. 5c), and geometric mean (Fig. 5d) approaches. This can be observed when considering the highest sidelobes in the standard CFDBF case located at $x = \pm 1$ m and $y \approx 1$ m, which are considerably attenuated by these three methods. Once again, the minimum value approach (Fig. 5e) provides the cleanest source map and eliminates most of the sidelobes presented for the baseline case. This source map is again comparable to the one obtained with the five synchronous arrays (with $N = 320$, see Fig. 5f).

Any potential variations in spatial resolution provided by each approach are difficult to observe directly in the source maps, so the calculated changes in the BW values for the *Synthetic case I* for each frequency are presented in Fig. 7a together with the expected Rayleigh resolution limit for the prototype array. The relative variations (in percentage) in the BW with respect to the standard CFDBF case are presented in Fig. 6b, where positive values denote an unwanted larger BW and vice versa. From the four methods studied, only the minimum value one can slightly reduce the BW (up to 4%) at low frequencies. The combined CSM, arithmetic mean, and geometric mean approaches suffer an increase in BW that is approximately the same for the three methods. These minor changes are expected as the BW is intrinsically related to the array aperture, and it does not benefit from a larger number of microphones acquired with the same aperture. For frequencies below 2 kHz, an approximate 4% increase in the BW is observed, whereas the frequency bands of 4 kHz and 8 kHz present a BW increase of around 8% and 16%, respectively. Most likely, the observed increase is a consequence of the decreasing effective array aperture caused by the oblique source directions [27] (i.e. those which do not correspond to the normal direction of the array at its center). This is precisely what happens when the prototype array is displaced in the y direction for the asynchronous measurements, and the averaging process of these three methods causes a slight increase of the final BW. For comparison purposes, the results of the five synchronous arrays ($N = 320$) are also plotted. The latter shows a consistent reduction in the BW, as expected from the larger array aperture of the final array. The graphs for this case are limited below 10 kHz due to the scan grid spacing and the considerably lower result obtained at this frequency is only caused by the limited spatial resolution for the BW estimations.

Fig. 7a depicts the MSL provided by each method considered. In general, higher frequencies show higher MSL values, as expected. The four methods tested provide consistently lower MSL values than the standard CFDBF baseline case. This is better shown in Fig. 7b, in which the relative MSL values with respect to the standard CFDBF case (ΔMSL) are presented. In this case, negative values represent a beneficial decrease of the MSL, i.e. an increase in the dynamic range. The results with the five synchronous arrays ($N = 320$) are also plotted for completeness. As also observed from the source maps, the minimum value approach offers the best results for the whole frequency range, reducing the highest sidelobe levels up to 4 dB and even presenting superior results than the five synchronous arrays for frequencies higher than 5 kHz. This agrees with the findings by Evans et al. [30], which proved that an increase in N_s while keeping the product NN_s constant (i.e. by decreasing the number of microphones per array) resulted in more favorable source maps. This trend held until the point that the prototype array did not have enough quality to properly locate the sound sources (i.e. N_s was very large but N too small). The other three techniques assessed follow a similar trend overall. The geometric mean presents a slightly higher reduction in the MSL, especially at frequencies higher than 2.5 kHz (offering an additional 3 dB MSL reduction with respect to the baseline) followed closely by the arithmetic mean and the combined CSM approaches.

The oscillations observed in the curves of Fig. 7 are caused by the frequency dependency of the sidelobes. At certain frequencies, the array locations selected have similar sidelobe locations, and the improvement provided by the combination of measurements is smaller. The results point to optimal array locations for the technique. These locations represent the maximum possible distance along the sidelobes, although such procedure is dependent on the frequency of interest and the array geometry. An array pairing method where the microphone distribution of each array used comes from an optimization procedure was proposed by

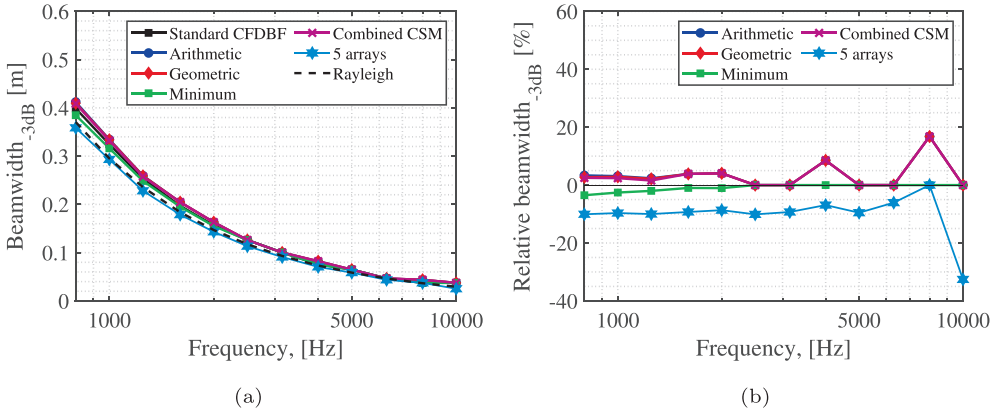

Fig. 6. (a) Comparison of the main lobe beamwidth (BW) 3 dB below its peak for the *Synthetic case I*. (b) Relative (in percentage) BW values with respect to the standard CFDBF case. All the combination methods had $N_s = 5$.

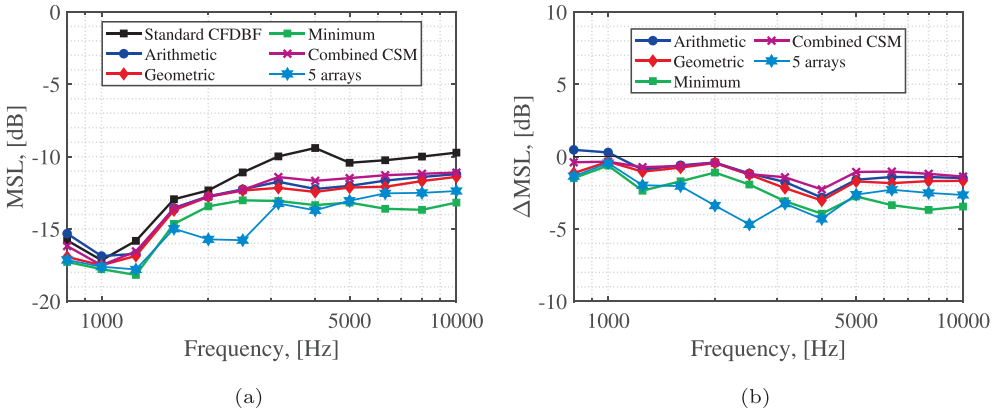

Fig. 7. (a) Maximum Sidelobe Level (MSL) comparison for the *Synthetic case I*. (b) Relative MSL values with respect to the standard CFDBF case. All the combination methods had $N_s = 5$.

Arcoundoulis et al. [63] for CFDBF and [85] for CLEAN-SC showing enhanced results. However, this technique requires the rearrangement of the microphones in different configurations, which is often not possible.

The average SL of the acoustic source maps within the selected scan grid is analyzed in Fig. 8a and the relative values with respect to the standard CFDBF case are included in Fig. 8b (where negative values denote *cleaner* source maps). The minimum value approach again provides the best performance with source maps with average SL values approximately 3 dB lower than the baseline. The other three techniques compared provide average SL results around 1 dB higher than the standard CFDBF. In other words, despite the reduction in MSL obtained, the combination of the maps leads to a slight overall *blur* of the lower sidelobes over a larger area, causing a more extended noise floor in the source map. Nevertheless, the positive effect of the reduction of the sidelobe

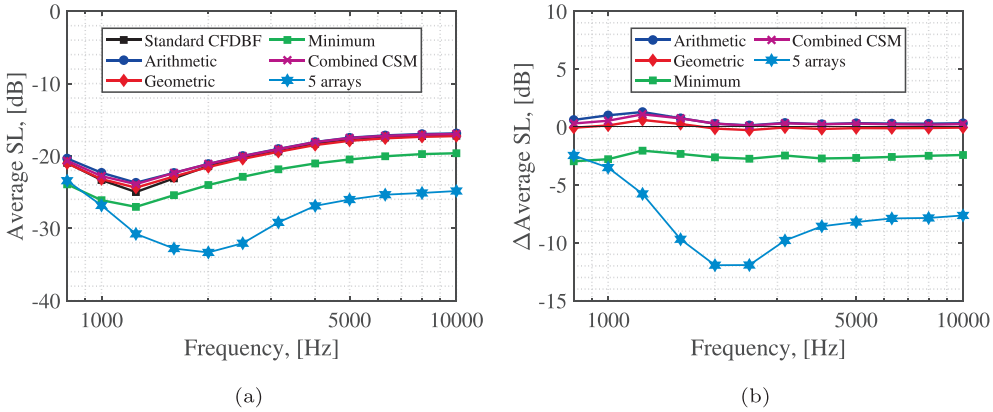

Fig. 8. (a) Average Sidelobe Level (SL) comparison for the *Synthetic case I*. (b) Relative average SL values with respect to the standard CFDBF case. All the combination methods had $N_s = 5$.

peaks is considered more relevant as they can be more easily misinterpreted as actual sources.

One typical challenge in acoustic imaging analyses is how to distinguish spurious sidelobes from actual secondary sources that have a L_p considerably lower than the peak value in the source map [66]. The *Synthetic case II* considers an additional secondary point source located at $(x, y, z) = (-0.75, 0.75, 0)$ m (see the green triangle marker in Figs. 1a and 9) with a L_p 12 dB lower than the first sound source from the *Synthetic case I*. Fig. 9a contains the acoustic source map obtained by the standard CFDBF, in which it is impossible to correctly identify the secondary source due to the presence of several sidelobes of similar level. The combined CSM (Fig. 9b), arithmetic mean (Fig. 9c), and geometric mean (Fig. 9d) improve the results by eliminating the other sidelobes around 12 dB lower but the shape of the secondary source is still contaminated with the sidelobes at that region. The minimum value approach (Fig. 9e) further enhances the source map by reducing the MSL and showing a comparable performance as the case with five synchronous arrays (Fig. 9f).

4.1.2. Experimental cases

As aforementioned, the setup of *Experimental case I* replicates that of the *Synthetic case I* in an anechoic environment. For the sake of conciseness, only the maps for the arithmetic and minimum value approach are shown in Fig. 10 at 2 and 4 kHz, analogously to the synthetic counterpart (Figs. 4 and 5. Despite the slightly poorer outcome due to minor experimental errors, the conclusions drawn for the *Synthetic case I* hold for the *Experimental case I*, i.e. the minimum value provides the best performance whereas the rest of the approaches perform worse.

Fig. 11a contains the BW results for all techniques, which follow the expected trend of the Rayleigh limit. The relative BW values (in percentage) with respect to the standard CFDBF case are shown in Fig. 11b. As in the test with synthetic data (see Fig. 6b), the arithmetic mean, geometric mean and combined CSM approaches suffer from an average 4% increase in the BW, although this time no peaks are observed at 4 kHz and 8 kHz. The same steep increase in BW for these three methods at 10 kHz is again seen due to poor spatial resolution, as in the synthetic case. It is observed that the geometric mean technique performs slightly better for frequencies above 4 kHz. On the other hand, the minimum value approach performs even better than in the synthetic case, reaching BW reductions up to 12% at high frequencies. The reasons for this difference are not yet known.

The MSL values for the *Experimental case I* are presented in Fig. 12a for all the methods considered. In general, higher MSL results are obtained with respect to the *Synthetic case I* (see Fig. 7) given the uncertainties of the experimental data, e.g. source nonconformity, room reflections, microphone phase loss, and errors during positioning. For example, the minimum MSL for the experimental case is about −16 dB, whereas values around −18 dB were observed for its synthetic counterpart. The remarkably higher MSL value reached at 800 Hz (about −6 dB) is due to the presence of a background noise source in the wind tunnel facility at that frequency band that contaminated the results and was considered as a sidelobe during the SL calculation procedure. The relative values with respect to the standard CFDBF are depicted in Fig. 12b. The minimum value approach again outperforms the rest of the methods, offering a MSL up to 3 dB lower. The sidelobe levels of the other three techniques are always above the values of the minimum value approach and perform comparably among each other, reaching ΔMSL values around −2 dB.

The average SL is also evaluated for the *Experimental case I*, resulting in Fig. 13a, and its relative values with respect to the standard CFDBF in Fig. 13b. As a reflection of the higher noise floor from the experimental case, the average SL results are slightly poorer for the experimental test. The minimum value approach is once again the best option with an average SL approximately 2 dB lower than the baseline. The other three techniques provide average SL values up to 1 dB higher than the standard CFDBF, in the same levels as the ones obtained for the synthetic case. The geometric mean method is slightly better than the other two approaches in this aspect.

The source maps for the flat plate tested in the open–jet wind tunnel corresponding to *Experimental case II* are included in Figs. 14 and 15 for one–third–octave bands centered at 2 kHz and 4 kHz, respectively. The smaller number of asynchronous measurements ($N_s = 3$ instead of 5) combined with the higher complexity of the

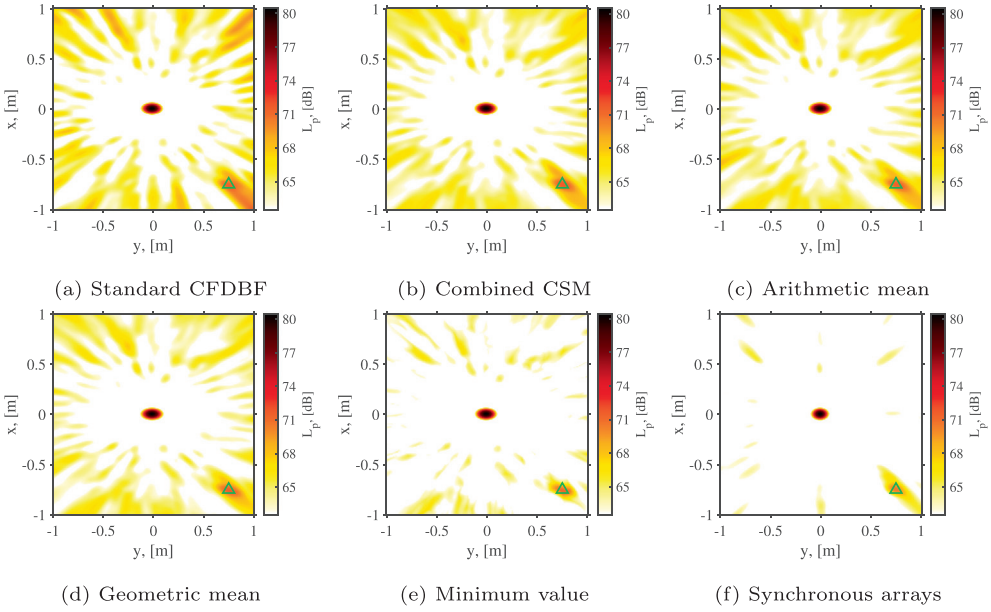

Fig. 9. Source maps for the *Synthetic case II* for the 4 kHz one–third–octave band. (a) Standard CFDBF, (b) Combined CSM, (c) Arithmetic mean, (d) Geometric mean, (e) Minimum value, (f) Synchronous arrays ($N = 320$). The △ symbol shows the position of the secondary synthetic sound source. All the combination methods had $N_s = 5$.

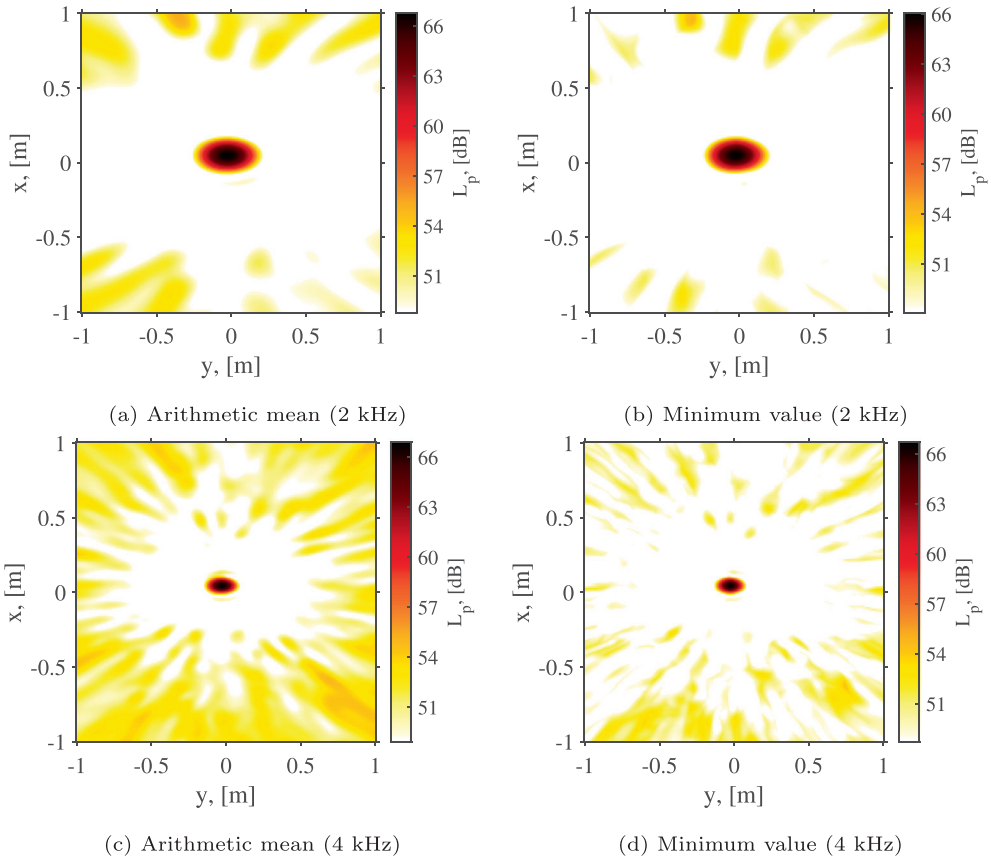

Fig. 10. Source maps for the *Experimental case I* for the 2 kHz (top row) and 4 kHz (bottom row) one–third–octave bands. (a and c) Arithmetic mean, (b and d) Minimum value. All the combination methods had $N_s = 5$.

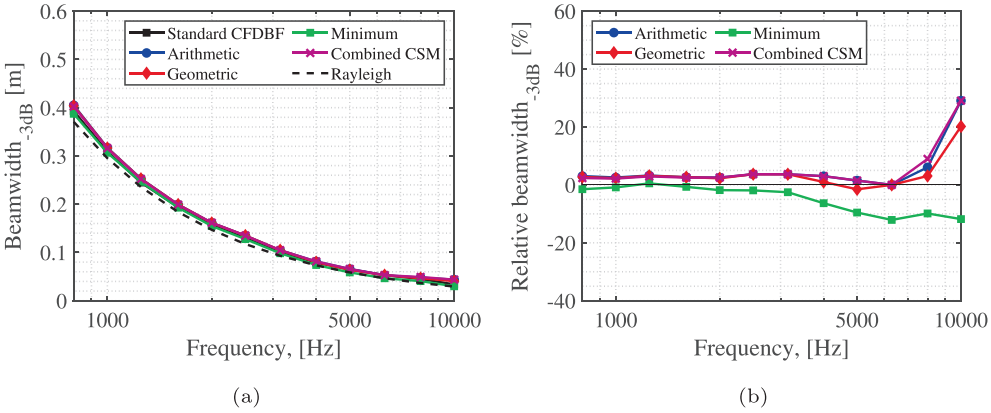

Fig. 11. (a) Comparison of the main lobe beamwidth (BW) 3 dB below its peak for the *Experimental case I*. (b) Relative (in percentage) BW values with respect to the standard CFDBF case. All the combination methods had $N_s = 5$.

sound source yields a less noticeable enhancement of the results from the four approaches.

The main improvement with respect to the baseline case is achieved by the minimum value approach (Figs. 14e and 15e), which renders a distributed line source between the support side plates, shorter than for the rest of the methods. This agrees with the expected source distribution since line sources longer than the span are most likely due to acoustic reflections because of the side plates or due to poor spatial resolution. Interestingly, for the 2 kHz case (Fig. 14e) two different line sources can be identified: one at the leading edge of the flat plate ($x \approx -0.6$ m) and another slightly more downstream ($x \approx -0.45$ m).

4.2. 3D source mapping

The use of combined asynchronous microphone array measurements also has an important appeal for 3D source mapping from planar arrays. Zamponi et al. [33] obtained cleaner source maps using a generalized inverse method for two different microphone arrays and combining the maps with a geometric mean approach.

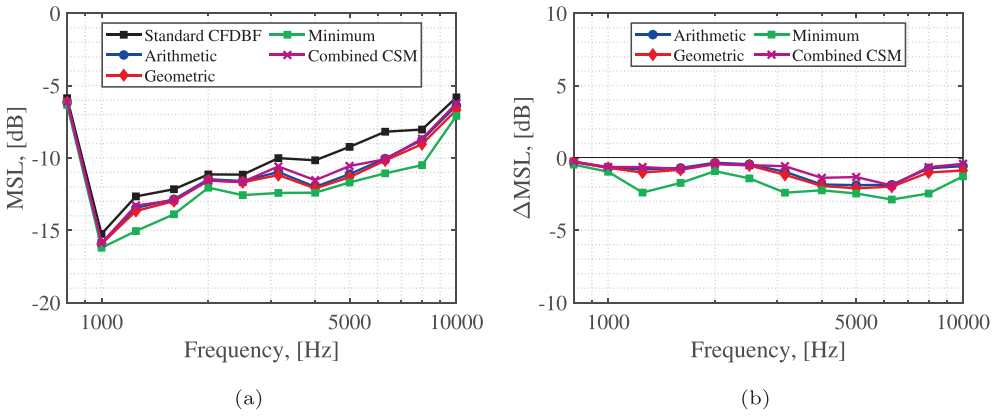

Fig. 12. (a) Maximum Sidelobe Level (MSL) comparison for the *Experimental case I*. (b) Relative MSL values with respect to the standard CFDBF case. All the combination methods had $N_s = 5$.

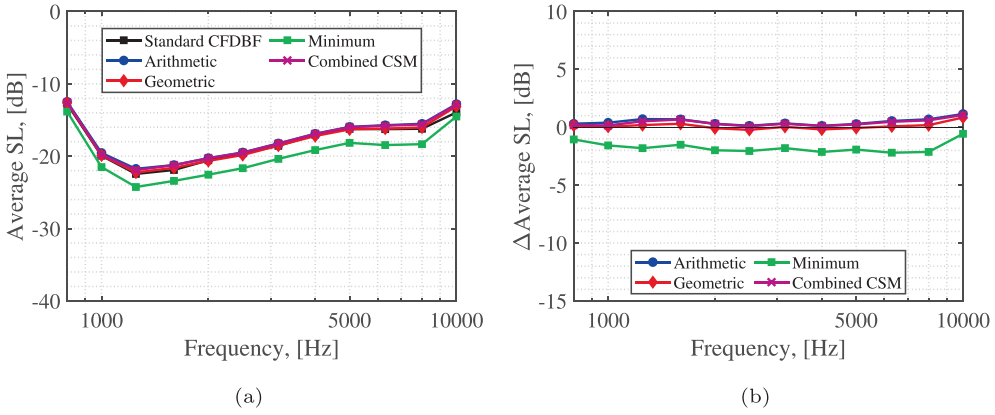

Fig. 13. (a) Average Sidelobe Level (SL) comparison for the *Experimental case I*. (b) Relative average SL values with respect to the standard CFDBF case. All the combination methods had $N_s = 5$.

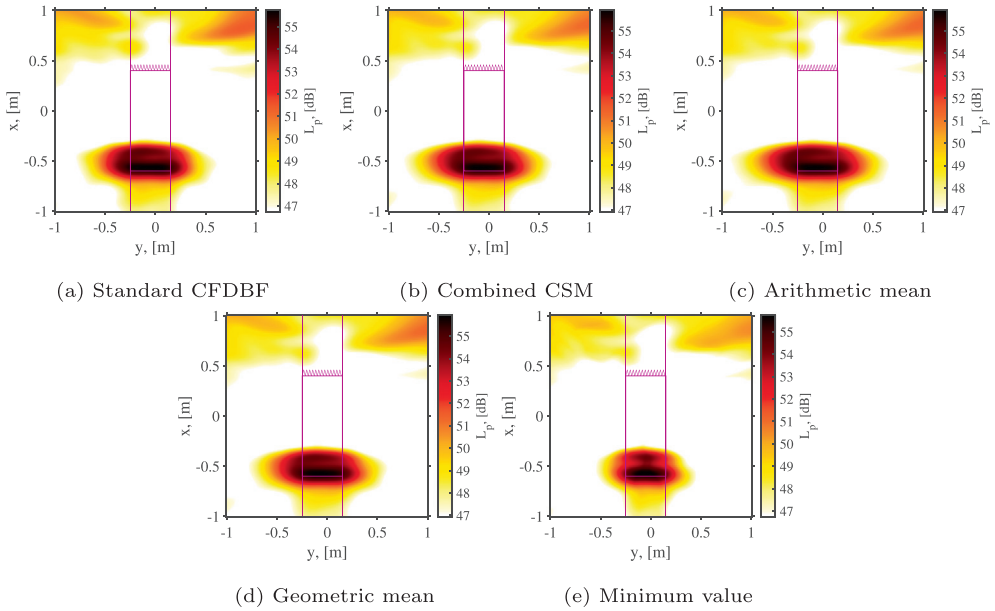

Fig. 14. Source maps for the *Experimental case II* for the 2 kHz one–third–octave band. (a) Standard CFDBF, (b) Combined CSM, (c) Arithmetic mean, (d) Geometric mean, (e) Minimum value. The solid magenta lines denote the flat plate and the support side plates. All the combination methods had $N_s = 3$.

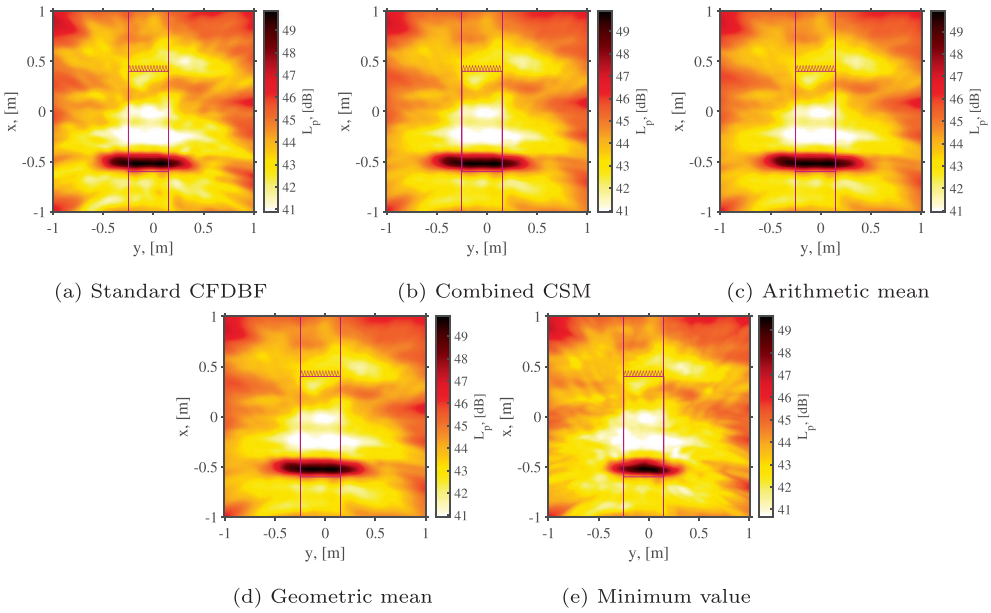

Fig. 15. Source maps for the *Experimental case II* for the 4 kHz one–third–octave band. (a) Standard CFDBF, (b) Combined CSM, (c) Arithmetic mean, (d) Geometric mean, (e) Minimum value. The solid magenta lines denote the flat plate and the support side plates. All the combination methods had $N_s = 3$.

The following results explore both numerically and experimentally the different methods tested before for the formation of a 3D source map.

4.2.1. Synthetic cases

Fig. 16 depicts the results of the volumetric source mapping for the *Synthetic case III* (i.e. an omnidirectional source located at $(x, y, z) = (0, 0, 0)$ m) obtained using two perpendicular array positions employing the different mentioned approaches. The iso–surfaces colors going from red to yellow represent levels 3, 6, 9, and 12 dB below the peak source level. Fig. 16a illustrates the resulting source map for 1 kHz using standard CFDBF on a single view. As expected, the main lobe is elongated in the direction normal to the array plane, due to the poorer resolution. The application of any of the combination approaches yields a separation of the approximate source location from the spurious levels away

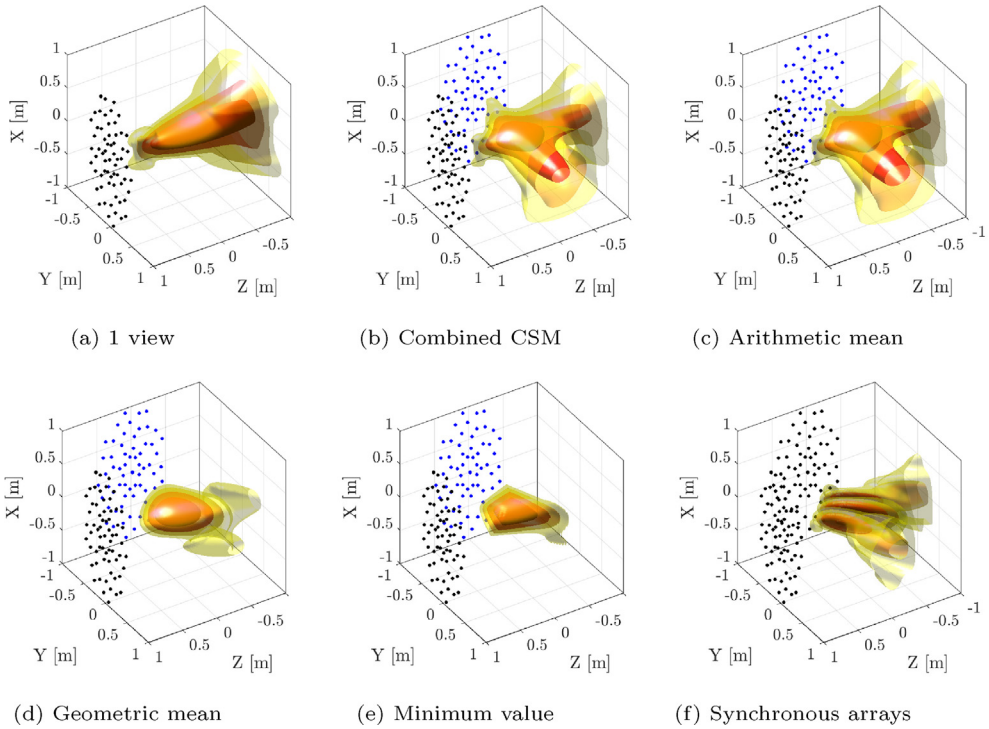

Fig. 16. 3D source maps for the *Synthetic case III* for the 1 kHz one–third–octave band. (a) Standard CFDBF, (b) Combined CSM, (c) Arithmetic mean, (d) Geometric mean, (e) Minimum value, (f) Synchronous arrays ($N = 128$). The maps show iso–surfaces of regions with L_p values 3, 6, 9 and 12 dB below the peak level. The microphone positions are denoted as dots. All the combination methods had $N_s = 2$.

from the array locations when considering levels 3 dB below the peak value. Those spurious sources are notably higher for the arithmetic mean approach (Fig. 16c) followed by the combined CSM procedure (Fig. 16b). Both techniques combine the beam patterns of both individual arrays and still present sidelobes away from the array positions for −9 and −12 dB. The geometric mean and the minimum value approaches (Figs. 16d and 16e, respectively) are able to completely suppress the spurious sources within the −12 dB range. Nevertheless, the minimum value approach presents the source with a slightly smaller BW in relation to the geometric mean. Fig. 16f contains the source map obtained when using 128 microphones (distributed in two equal sub–arrays perpendicular to each other) synchronously in a single measurement, which presents a smaller BW than the rest of the cases, but a sidelobe pattern around −6 dB elongated along the bisector angle of the two planes containing the sub–arrays. In general, at this relatively low frequency, it is apparent how using multiple views is effective in reducing the higher levels predicted for mapping points far away in the array normal axis.

The same results are presented for a higher frequency (4 kHz) in Fig. 17. Contrary to the previous case, where a single source is observed for the single view process, the map obtained for this case is contaminated by multiple sidelobes within the −12 dB dynamic range that create the impression of several sound sources present. Among the different combination methodologies to compose the 3D source mapping, the geometric mean (Fig. 17d), and the minimum value (Fig. 17e) can almost completely remove the spurious sources from the 12 dB range and restrict the main lobe to an ellipsoid. On the other hand, the combined CSM and the arithmetic mean approaches (Figs. 17b and 17c) offer a noisier map, with sidelobes still present around the real source location. The case with two synchronous arrays ($N = 128$, Fig. 17f) yields a smaller main lobe but still presents the aforementioned sidelobe level pattern 6 dB below the maximum value along the bisector angle direction. Overall, the increasing number of microphones simulated in the synchronous array does not seem to help in the suppression of the sidelobes. Nevertheless, a 3D array still has a larger aperture, yielding a smaller beamwidth.

The effects of the four different approaches in the obtained 3D maps can be observed in the changes of the BW and MSL measured at different frequencies (Fig. 18).

The changes in BW, estimated from the volume of the main lobe iso–surface at 3 dB below the map's maxima, are displayed in Fig. 18a. The results from the combined array measurements lie in between the predicted results from the Rayleigh criteria for planar arrays and the synchronous result of the two array positions used. Results indicate that the combination of asynchronous measurements cannot reduce the BW to the levels of the synchronous measurements at low frequencies, given that the real aperture of the array is not changing. Nevertheless, the approaches can perform well for high–frequency measurements, where the array's aperture is already larger than the acoustic wavelengths. Among the methodologies, the minimum value approach performs best overall and presents an estimated BW about 30% higher than the synchronous measurements. The geometrical mean, combined CSM and arithmetic mean have slightly worse performances, with the latter presenting the highest BW.

Nevertheless, the Maximum Sidelobe Level (MSL) shows the main advantages of the combined–measurements in relation to the single measurement (Fig. 18b). The different views can significantly reduce the sidelobe levels, even below the values of the synchronous measurement. Again, within the methods, the minimum value approach is the one that performs best, especially at high frequencies. As observed in Figs. 16 and 17, the synchronous measurement suffers from high sidelobe levels in the surroundings of the main lobe. These sidelobes are suppressed by the combined measurements as the BW is enlarged. This behavior causes the MSL for all the combination approaches to be higher than for the synchronous case for lower frequencies, whereas at higher frequencies, the synchronous measurement outperforms the combined

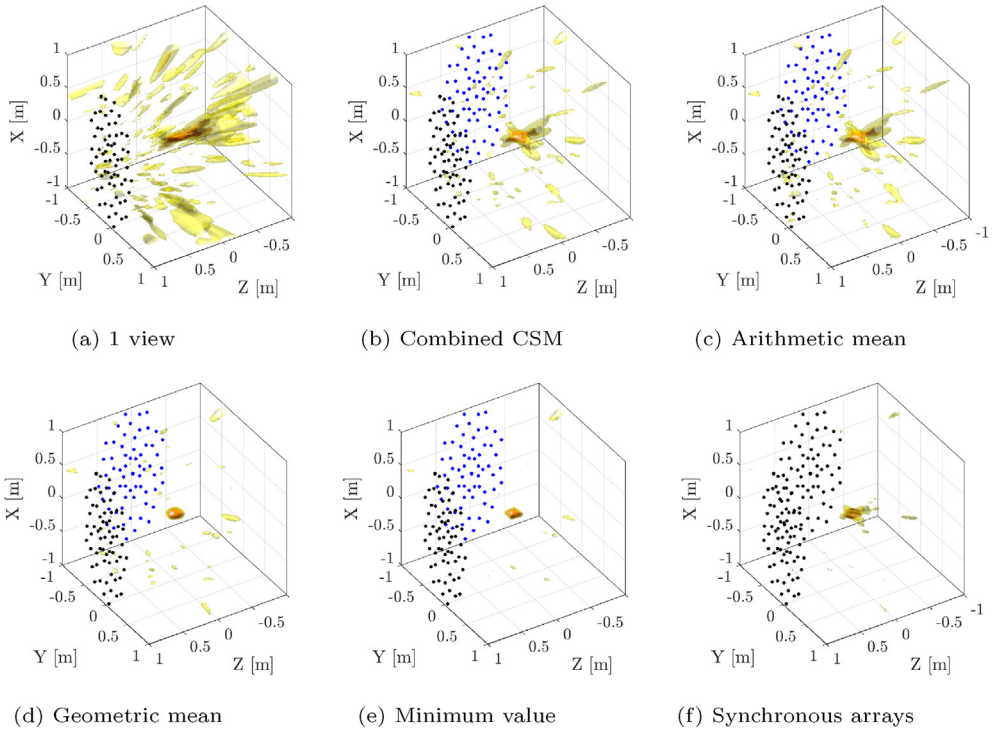

Fig. 17. 3D source maps for the *Synthetic case III* for the 4 kHz one–third–octave band. (a) Standard CFDBF, (b) Combined CSM, (c) Arithmetic mean, (d) Geometric mean, (e) Minimum value, (f) Synchronous arrays ($N = 128$). The maps show iso–surfaces of regions with L_p values 3, 6, 9 and 12 dB below the peak level. The microphone positions are denoted as dots. All the combination methods had $N_s = 2$.

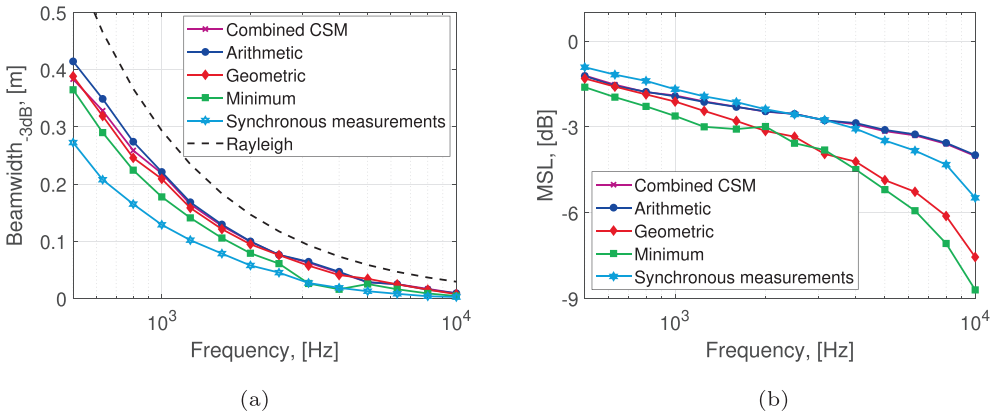

Fig. 18. Comparison between (a) Beamwidth (BW) 3 dB below the peak, and (b) Maximum Sidelobe Level (MSL) estimated from the *Synthetic case III*. All the combination methods had $N_s = 2$.

CSM and arithmetic mean approaches. Still, the geometric mean and the minimum value approach have lower MSL levels in comparison to the synchronous measurements.

4.2.2. Experimental cases

The *Experimental case I* reproduces the single source case explored in Section 4.2.1 in an anechoic environment. Figs. 19 and 20 show the obtained source maps from the different combining approaches explored. The real environment hampers the quality of the overall results, evidenced by the higher presence of spurious sources 12 dB below the peak for the case of 4 kHz (compared with Fig. 17).

At 1 kHz (Fig. 19), the main effect of the multiple views is the reduction of the main lobe by the combined view. Among the methodologies tested, the geometric mean (Fig. 19d), and minimum value approach (Fig. 19e) completely eliminate the sidelobes within the mapping region. The combined CSM approach (Fig. 19b) and the arithmetic mean (Fig. 19c) can partially reduce the side sources, creating a clear definition of the centre source within a 3 dB dynamic range.

At higher frequencies, such as 4 kHz (see Fig. 20), the dominating source of errors are the sidelobes. Still, the correct identification of the main source is accomplished by all the methods applied. Overall, the shape of the main lobe agrees with the *Synthetic case III*, with a higher amount of sidelobes appearing at levels 12 dB bellow the source level. The minimum value approach (Fig. 20e) deals with the spurious sources in a better manner providing the cleanest map, followed by the geometric mean

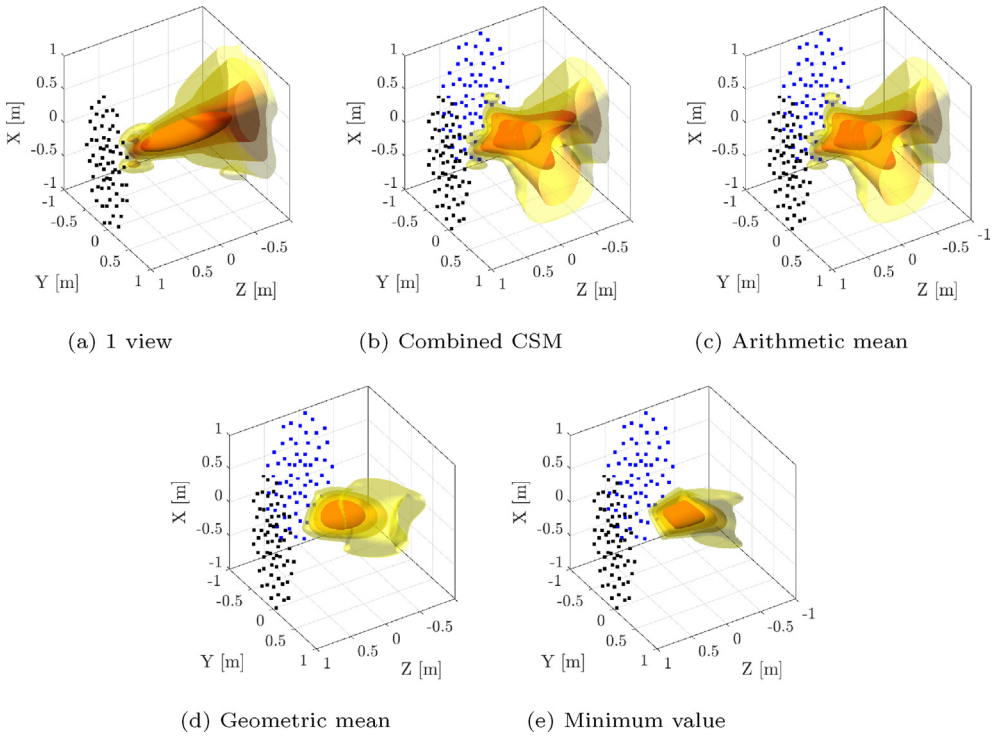

Fig. 19. 3D source maps for the *Experimental case I* for the 1 kHz one–third–octave band. (a) Standard CFDBF, (b) Combined CSM, (c) Arithmetic mean, (d) Geometric mean, (e) Minimum value. The maps show iso–surfaces of regions with L_p values 3, 6, 9 and 12 dB below the peak. The microphone positions are denoted as dots. All the combination methods had $N_s = 2$.

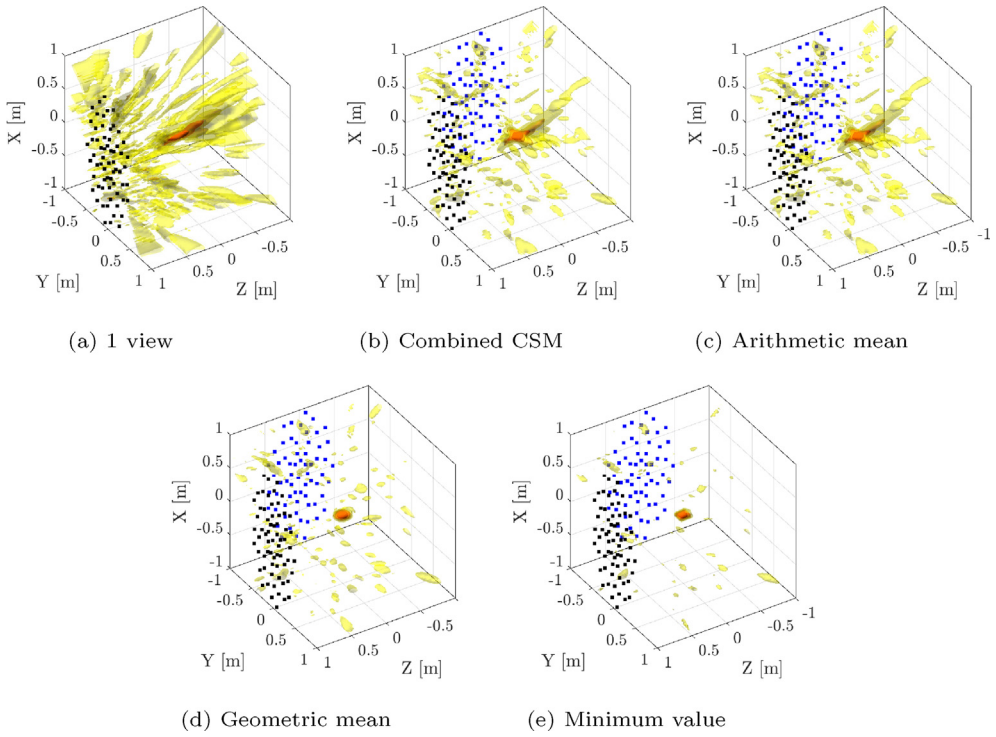

Fig. 20. 3D source maps for the *Experimental case I* for the 4 kHz one–third–octave band. (a) Standard CFDBF, (b) Combined CSM, (c) Arithmetic mean, (d) Geometric mean, (e) Minimum value. The maps show iso–surfaces of regions with L_p values 3, 6, 9 and 12 dB below the peak. The microphone positions are denoted as dots. All the combination methods had $N_s = 2$.

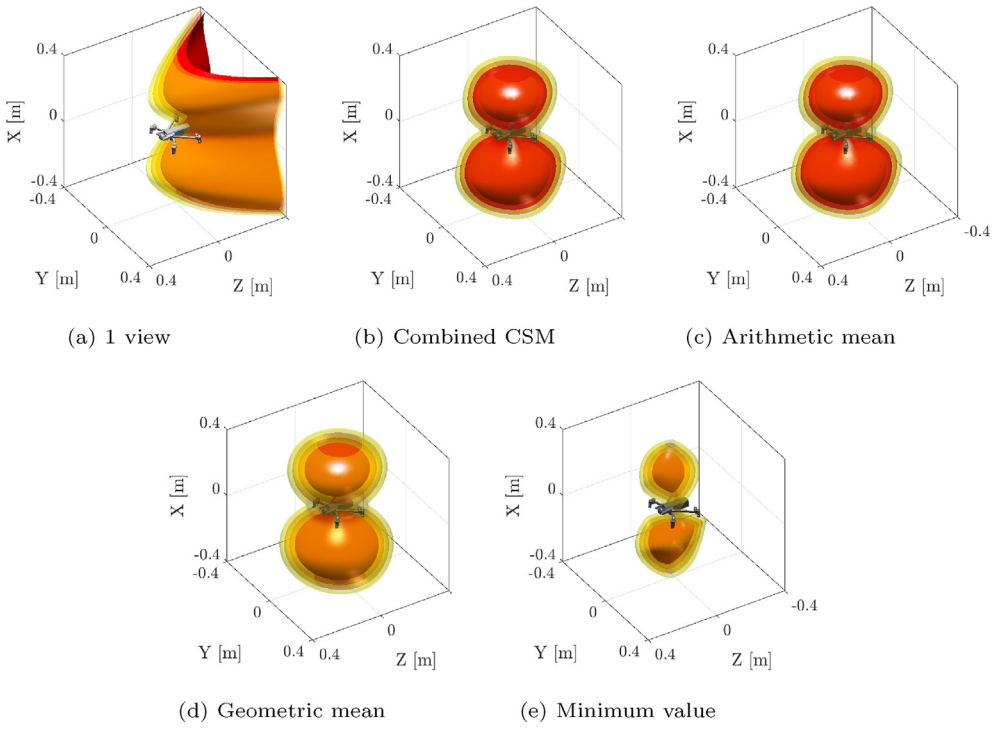

Fig. 21. 3D source maps for the *Experimental case III* for the 1 kHz one–third–octave band. (a) single measurement (b) Combined CSM, (c) Arithmetic mean, (d) Geometric mean, (e) Minimum value. The maps show two iso–surfaces of regions with L_p values 3, 6, 9, and 12 dB below the peak. All the combination methods had $N_s = 4$.

(Fig. 20d). The combined CSM (Fig. 20d) and the arithmetic mean (Fig. 20c) offer similar map results.

The experimental case featuring a hovering drone (*Experimental case III*) presents a complex sound field consisting of several noise sources of broadband and tonal nature at different locations in respect to the array plane. Therefore, this example is an application case that would benefit from a combined 3D mapping technique. Fig. 21 contains the obtained results from the combination of the

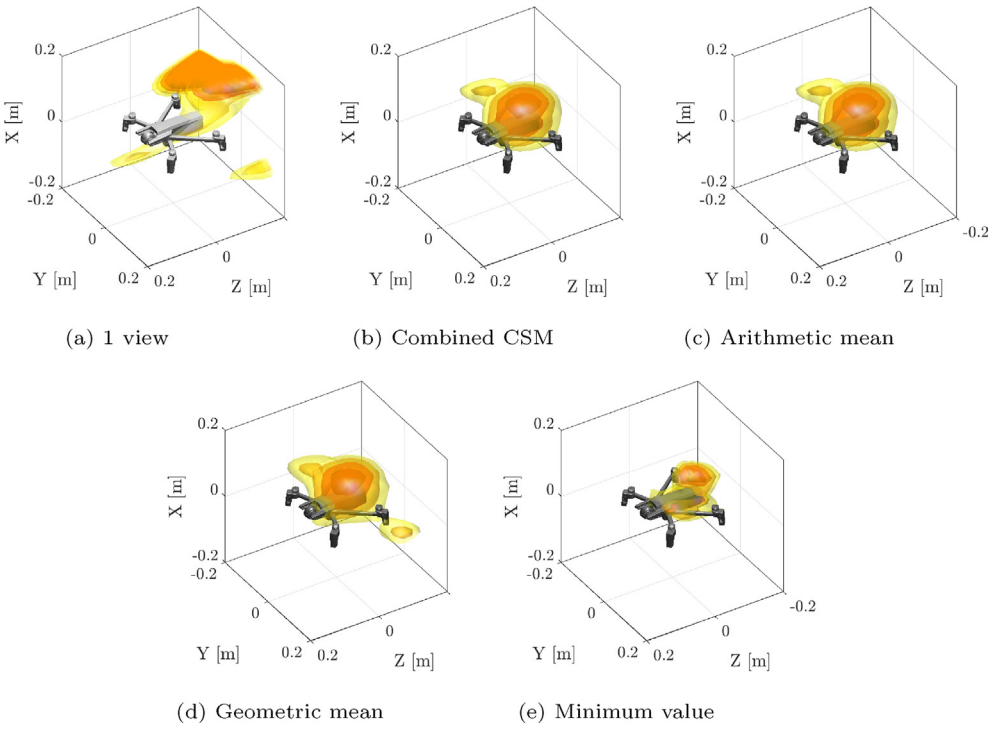

Fig. 22. 3D source maps for the *Experimental case III* for the narrowband frequency of 3600 Hz. (a) single measurement (b) Combined CSM, (c) Arithmetic mean, (d) Geometric mean, (e) Minimum value. The maps show two iso–surfaces of regions with L_p values 3, 6, 9, and 12 dB below the peak. All the combination methods had $N_s = 4$.

four different measurements for a one–third–octave band centered at 1 kHz. The case with a single measurement is also included in Fig. 21 and presents a similar elongated lobe behavior as for the omnidirectional source in Figs. 19a and 20a. At such frequency and for the combined approaches, the overall noise from the drone is seen as a compact source, resembling the two lobes from a dipole. This can be observed from the combined CSM (Fig. 21), arithmetic mean (Fig. 21b), and geometric mean (Fig. 21c), all presenting lobes of similar size. A similar noise radiation pattern was also reported in the literature [86] for a comparable drone model. The characteristic cleaner results from the minimum value approach (Fig. 21d) reduce the lobes in relation to the combined CSM and geometric mean, resulting in a less smoothed shape. This result shows that applying the minimum value approach to a sound source that is not perfectly omnidirectional would benefit certain emission angles when calculating the source map, and may lead to such skewed lobe shapes.

At a higher frequency (3.6 kHz), the different sources of noise in the drone can be observed (Fig. 22). Without the different views, no relevant source can be identified (Fig. 22a). The combination of the different views seems to show two different sources, i.e. a main noise source located close to the drone's internal cooling fan, and two weaker sources from the rear propellers. All the sources can be captured by the geometric mean approach (Fig. 22d), while only one propeller and the internal cooling fan are detected by the combined CSM and arithmetic mean approaches (Figs. 22b, and 22c). It is interesting to notice that the minimum value approach (Fig. 22e) can only identify the internal cooling fan source. The propeller sources are probably weaker in some of the different views used and, therefore, the minimum value approach suppresses the contributions of these sources.

It is important to note that this practical application case should only be considered as indicative since the control system of this type of drone is very sensitive to small gusts or air movements which can modify the propeller rotational speeds to maintain the drone steady. As such, small differences could occur between the noise emissions of the different asynchronous array measurements.

5. Conclusions

The possibility of combining several asynchronous microphone array measurements is investigated for both improving the results of two–dimensional source maps and to allow the mapping of sources within a 3D field. Four different techniques for combining the results from the multiple asynchronous array measurements are tested. Three of them consist of combining the mapped sources according to different rules (namely the arithmetic and geometric means, and the minimum of the values), and a fourth one obtained from the combination of the CSM of all measurements, neglecting the cross–correlations among different views.

The techniques are tested for simple synthetic cases (monopole sound sources placed within the scan domain) and for experimental cases, ranging from a model speaker located within an anechoic environment to an aeroacoustic uncorrelated line source and a hovering quadcopter drone.

For two–dimensional source maps, the use of multiple array views is seen to impact mainly on the suppression of the sidelobes. The beamwidth is mildly affected and, for some conditions, the consequent mapping from a non–centered array in relation to the source can even slightly increase the size of the main lobe. In general, the sidelobe levels further decrease as the number of asynchronous measurements is increased with the consequent increase in measurement and computational time, see Appendix A for more information. Among the different methods, the minimum value approach outperforms the others, reducing the sidelobe levels as much as 5 dB for a combination of 9 views in comparison to the standard single–measurement case, see Fig. A.1b. The other methods perform similarly in levels, with a slight advantage obtained by the geometric mean in relation to the combined CSM and arithmetic mean approaches.

In order to assemble a 3D source map, array views from different angles are necessary. The 3D maps obtained from a single view are extremely restricted along the array's normal direction. The addition of a second view is, in many cases, sufficient for the distinction of the main sources within the interrogation volume. At low frequencies, the multiple views will mostly reduce the size of the main lobe. As the frequency increases, the beamwidth is limited by the aperture of the single array and the main effect of the multiple views is the reduction of the sidelobe level. Again, the minimum value approach provides the cleanest maps. It is found that about 4 views rotated along the center of the source yield a good improvement in the captured source beamwidth, see Appendix A.

Nevertheless, the advantages of the minimum value approach must be taken with care as it considers that the source does not change its emissions within the different views. This very restrictive character can lead to significant errors in the level estimation, especially when sources with a different directivity pattern than the steering vector considered are analyzed, as observed for the measurements with the hovering drone case.

Appendix A discusses the advantages obtained when increasing the number of asynchronous measurements N_s. This parameter is mostly limited by practical constraints, such as the available space to displace the array within the experimental facility or the additional measuring and computational time required. In case a large value of N_s is desired, mounting the microphone array on a moving traverse system could provide a simple measurement setup.

CRediT authorship contribution statement

Lourenço Tércio Lima Pereira: Writing - original draft, Methodology, Formal analysis, Writing - review & editing. **Roberto Merino-Martínez:** Writing - original draft, Methodology, Formal analysis, Writing - review & editing. **Daniele Ragni:** Supervision, Writing - review & editing. **David Gómez-Ariza:** Writing - review & editing. **Mirjam Snellen:** Supervision, Writing - review & editing.

Declaration of Competing Interest

The authors declare that they have no known competing financial interests or personal relationships that could have appeared to influence the work reported in this paper.

Acknowledgments

The authors would like to kindly thank Edoardo Grande for his help during the experimental campaign and his constructive comments and feedback.

Appendix A. Influence of the number of asynchronous measurements

An important aspect to consider is the influence of the number of asynchronous measurements (N_s) on the potential quality enhancement of the acoustic source maps.

To study this, firstly, the 2D analysis of the *Synthetic case I* was extended to additional cases with other N_s values with symmetric array displacements with respect to $y = 0$, see Table A.1.

Fig. A.1 discusses the influence of N_s in the relative differences of the 2D source maps obtained for the four approaches considered with respect to the standard CFDBF. The results corresponding to the case with five synchronous arrays ($N = 320$) discussed before are also plotted for comparison. The values included in Fig. A.1 correspond to the 4 kHz one–third–octave band, but other frequencies

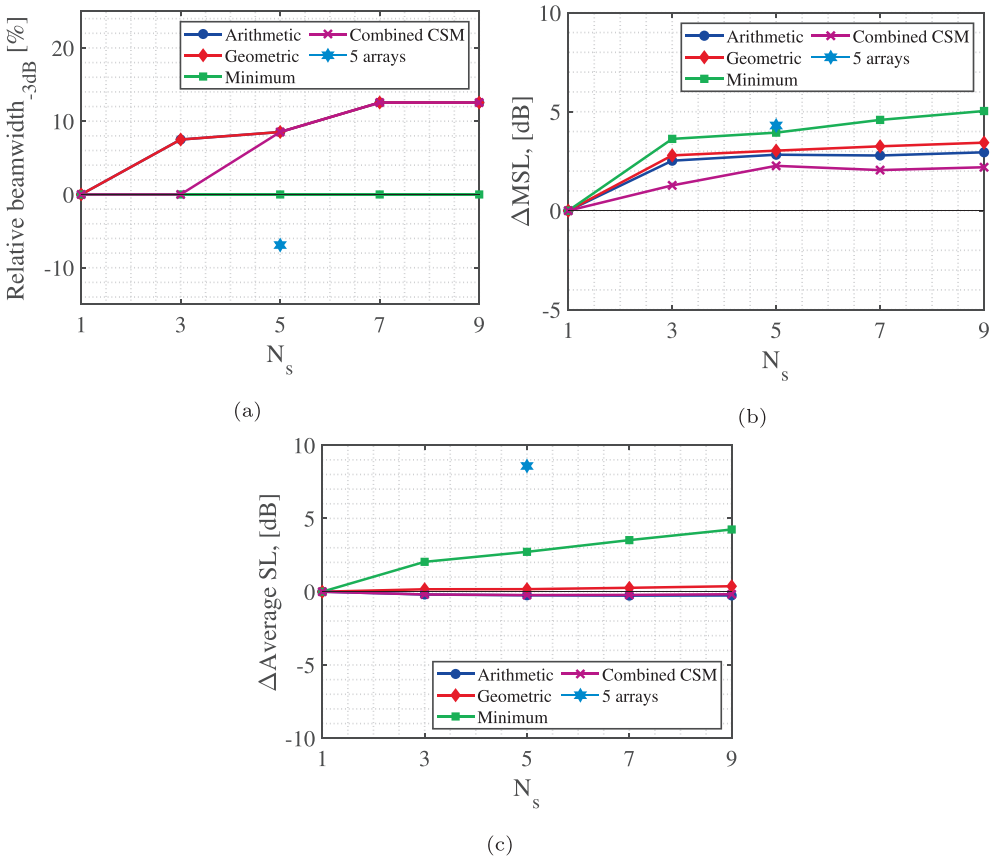

Fig. A.1. Influence of the number of asynchronous measurements N_s for the *Synthetic case I* for the 4 kHz one–third–octave band on the parameters (with respect to the standard CFDBF case): (a) relative BW (in percentage), (b) relative MSL, and (c) relative average SL.

Table A.1
Virtual displacements of the microphone array for the 2D analysis of the *Synthetic case I*.

N_s	Displacements in the y direction, [mm]
1	0 (prototype array)
3	±150
5	±150 and ±300 (case considered in Section 4.1)
7	±150, ±300, and ±450
9	±150, ±300, ±450, and ±600

showed comparable behaviors. This frequency band represents one of the worst cases for the relative BW parameter for the arithmetic mean, geometric mean, and combined CSM approaches (see Fig. 6) with relative BW increases of about 10% and, observing Fig. A.1a, it seems that these three techniques suffer from slightly greater BW as N_s increases. This behavior agrees with the hypothesis made that the effective array aperture is decreased when using the array in oblique directions, as mentioned in Section 4.1. Thus, there is a trade–off between the MSL and the BW. The relative BW of the minimum value approach does not seem to vary with N_s and it remains close to zero (i.e. the same as for standard CFDBF).

The relative MSL (see Fig. A.1b), on the other hand, seems to increase gradually with N_s for all methods. The minimum value approach even reaches higher ΔMSL values larger than the case with five synchronous arrays for $N_s \geqslant 7$.

Lastly, the improvement of the relative average SL (see Fig. A.1c) provided by the minimum value approach seems to increase linearly with N_s, reaching values of 4.2 dB for $N_s = 9$. The other three techniques do not provide major changes with respect to the standard CFDBF case and remain within values within ±0.5 dB.

For all the test cases considered for 2D source mapping, the prototype array was only displaced in the y direction for simplicity and practical reasons. It should be noted that, if the setup allows for it, moving the prototype array in other dimensions (especially also in the x direction for 2D source mapping) would further improve the performance of the techniques described in Section 2 since that would provide additional points of view with significantly different sidelobe patterns [50]. Besides, the consequences of mapping of a non–centered source observed in A.1a can be avoided by rotating the array around the source location instead of simply translating the array.

For the case of 3D source mapping, additional array positions were considered for the *Synthetic case III*. Figs. A.2–A.6 present the source maps for 1 kHz obtained by the different approaches when N_s (i.e. the number of points of view) is set to 3, 4, and 6 by rotating the array an angle of $\frac{360°}{N_s}$ along the x axis. The graphs show how consistently increasing N_s improves the source location, especially at low levels, e.g. 12 dB below the peak value. At this level, the combined CSM (Fig. A.2) and arithmetic mean (Fig. A.3) approaches at 1 kHz present sidelobe levels that exceed the beamforming domain, limiting the dynamic range of the analysis. The other two approaches (geometric mean, Fig. A.4 and minimum value, Fig. A.5) yield a better resolution of the source main lobe limits for all number of views provided. Nevertheless, the solutions for $N_s = 3$ still present a larger main lobe, that converges to an ellipsoidal shape for the cases more than 4 views. The resulting maps for synchronous measurements (Fig. A.6), i.e. considering

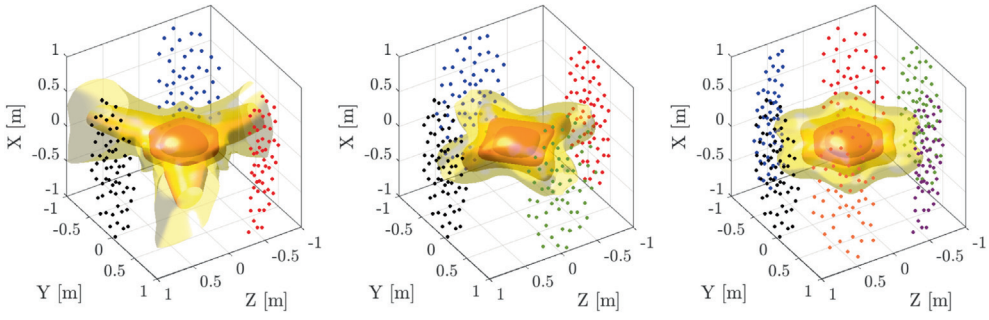

(a) $N_s = 3$ (b) $N_s = 4$ (c) $N_s = 6$

Fig. A.2. 3D source maps for the *Synthetic case III* at 1 kHz using 3, 4 and 6 views for the combined CSM approach (a, b, and c respectively). The iso–surfaces of regions with L_p 3, 6, 9, and 12 dB below the peak are presented. The microphone positions are denoted as dots.

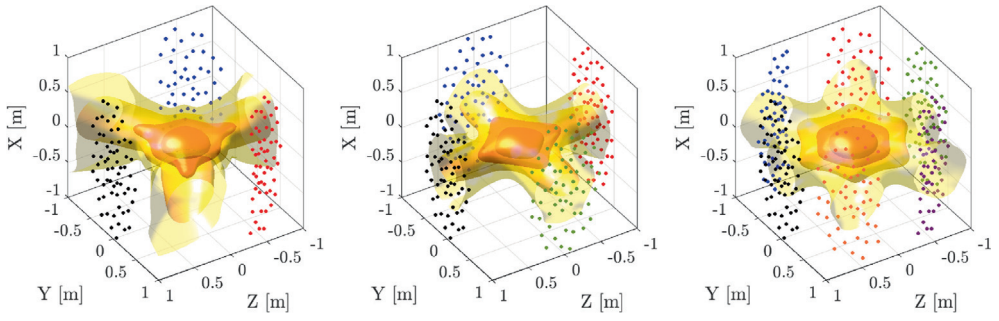

(a) $N_s = 3$ (b) $N_s = 4$ (c) $N_s = 6$

Fig. A.3. 3D source maps for the *Synthetic case III* at 1 kHz using 3, 4 and 6 views for the arithmetic mean approach (a, b, and c respectively). The iso–surfaces of regions with L_p 3, 6, 9, and 12 dB below the peak are presented. The microphone positions are denoted as dots.

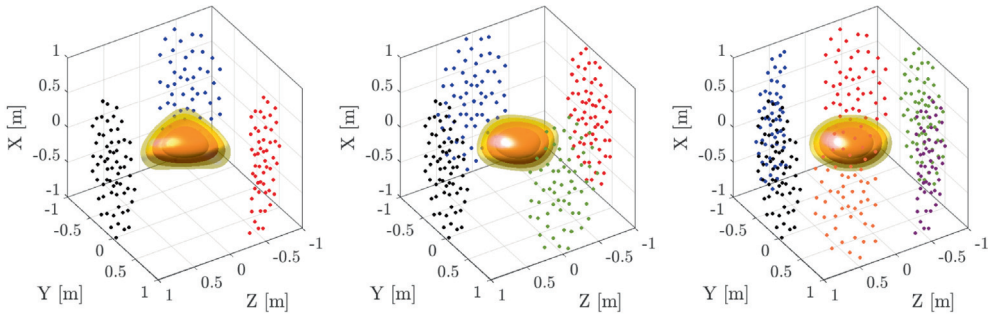

(a) $N_s = 3$ (b) $N_s = 4$ (c) $N_s = 6$

Fig. A.4. 3D source maps for the *Synthetic case III* at 1 kHz using 3, 4 and 6 views for the geometric mean approach (a, b, and c respectively). The iso–surfaces of regions with L_p 3, 6, 9, and 12 dB below the peak are presented. The microphone positions are denoted as dots.

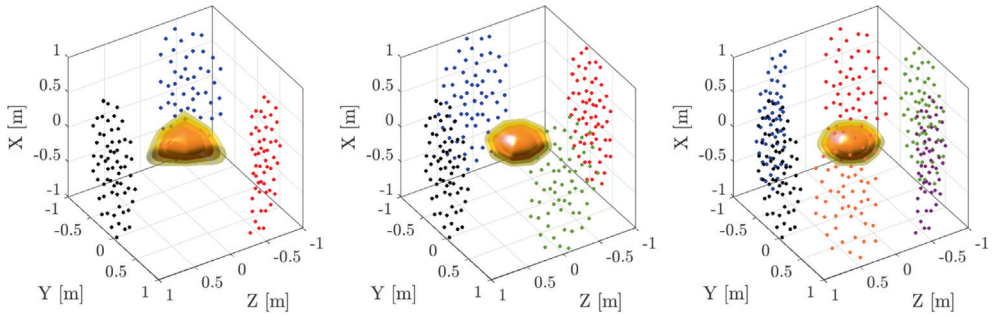

(a) $N_s = 3$ (b) $N_s = 4$ (c) $N_s = 6$

Fig. A.5. 3D source maps for the *Synthetic case III* at 1 kHz using 3, 4 and 6 views for the minimum value approach (a, b, and c respectively). The iso–surfaces of regions with L_p 3, 6, 9, and 12 dB below the peak are presented. The microphone positions are denoted as dots.

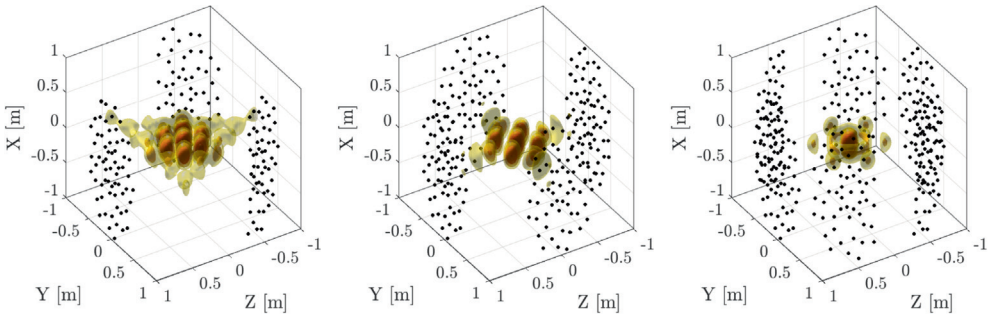

(a) $N_s = 3$ (b) $N_s = 4$ (c) $N_s = 6$

Fig. A.6. 3D source maps for the *Synthetic case III* at 1 kHz using 3, 4 and 6 views for equivalent synchronous measurements (a, b, and c respectively). The iso–surfaces of regions with L_p 3, 6, 9, and 12 dB below the peak are presented. The microphone positions are denoted as dots.

192 ($N_s = 3$), 256 ($N_s = 4$), and 384 ($N_s = 6$) microphones at the same array locations as for the asynchronous ones, yield a significantly smaller main lobe, but with the presence of several sidelobes. The sidelobes reach levels of up to -3 dB for $N_s = 3$ and are reduced for $N_s = 4$ (-6 dB) and $N_s = 6$ (-9 dB).

For the case of 4 kHz (Figs. A.7–A.11), the trends are similar, although the smaller beamwidths make all isocontours restricted within a sphere of 0.5 m radius centered at the source location. Spurious sidelobes are only observed for the arithmetic mean and combined CSM approaches (Figs. A.7 and A.8, respectively). Nevertheless, the sidelobes are captured at the borders of the domain and are apart from the surroundings of the source. The synchronous measurements (Fig. A.11) again yield a smaller beamwidth with the cost of stronger sidelobes.

The variation of the beamwidth shown in Fig. A.12 with the number of asynchronous measurements shows the necessary number of rotations that one can apply until the beamwidth and, consequently, the map of the main lobe does not vary significantly. At both frequencies (1 kHz and 4 kHz) a mapping with at least 4 views seems to suffice in order to converge the minimum BW for

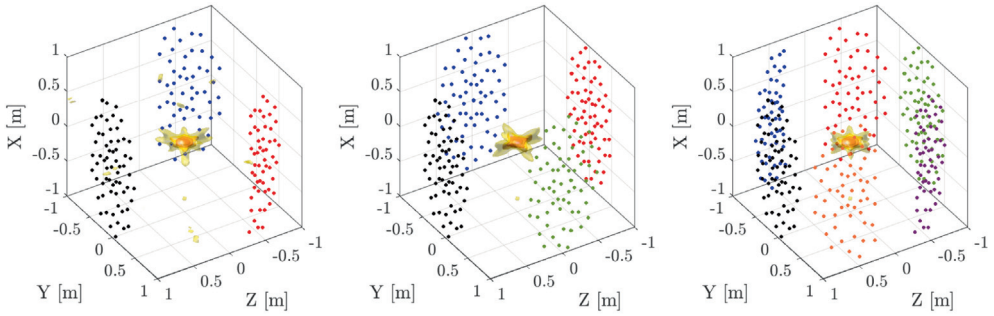

(a) $N_s = 3$ (b) $N_s = 4$ (c) $N_s = 6$

Fig. A.7. 3D source maps for the *Synthetic case III* at 4 kHz using 3, 4 and 6 views for the combined CSM approach (a, b, and c respectively). The iso–surfaces of regions with L_p 3, 6, 9, and 12 dB below the peak are presented. The microphone positions are denoted as dots.

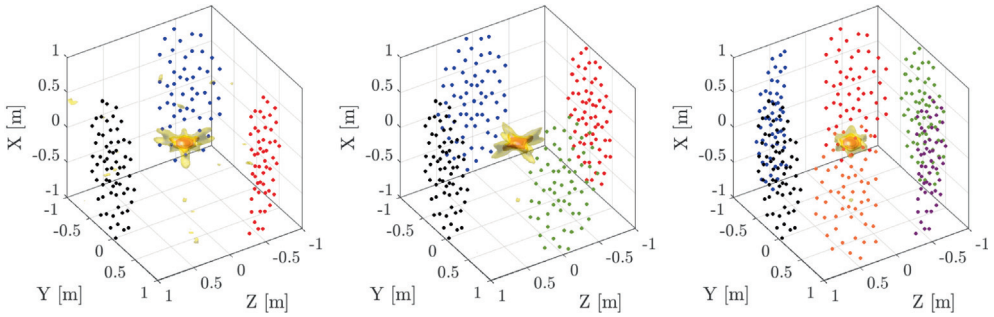

(a) $N_s = 3$ (b) $N_s = 4$ (c) $N_s = 6$

Fig. A.8. 3D source maps for the *Synthetic case III* at 4 kHz using 3, 4 and 6 views for the arithmetic mean approach (a, b, and c respectively). The iso–surfaces of regions with L_p 3, 6, 9, and 12 dB below the peak are presented. The microphone positions are denoted as dots.

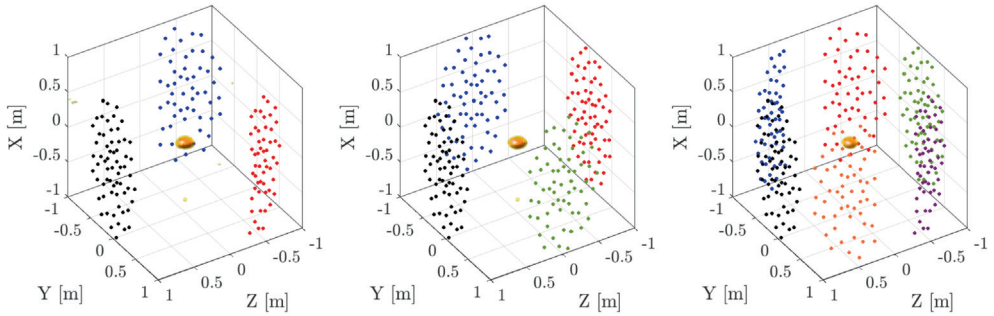

(a) $N_s = 3$ (b) $N_s = 4$ (c) $N_s = 6$

Fig. A.9. 3D source maps for the *Synthetic case III* at 4 kHz using 3, 4 and 6 views for the geometric mean approach (a, b, and c respectively). The iso–surfaces of regions with L_p 3, 6, 9, and 12 dB below the peak are presented. The microphone positions are denoted as dots.

all the techniques. The BW value of convergence is affected by the technique selected. The minimum value approach will converge to a significantly lower level than all the other techniques. The geometric mean technique presents slightly smaller values than the arithmetic and the combined CSM approaches. As discussed, neither of the techniques are comparable to the synchronous measurements using a full microphone array. Nevertheless, this approach will increase significantly the cost of the array and acquisition equipment while still presenting sidelobes that may affect the overall interpretation of the resulting source map.

Due to the advantages obtained when increasing N_s, installing the microphone array in an automatic traversing system could be beneficial in case a large value of N_s is desired. For applications with rotating sound sources, a continuously rotating array can also improve the obtained results [11,47], provided that the rotational speed is low enough not to cause disturbances in the microphone recordings or aerodynamic noise.

A potential upper limit for N_s may be determined by practical constraints, such as the available space to displace the array within the experimental facility or the time required for positioning the

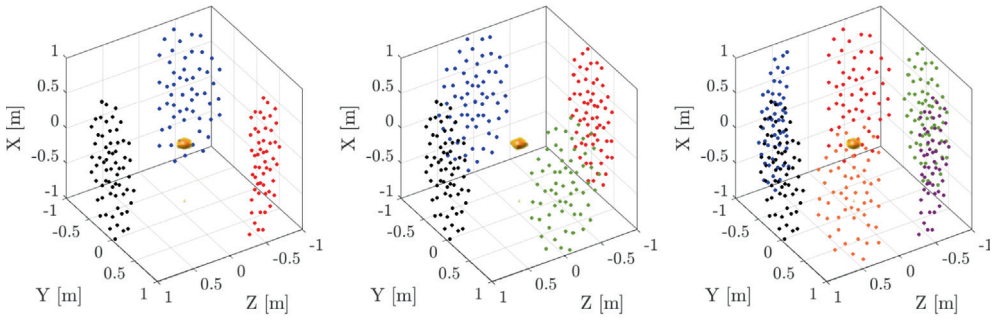

(a) $N_s = 3$ (b) $N_s = 4$ (c) $N_s = 6$

Fig. A.10. 3D source maps for the *Synthetic case III* at 4 kHz using 3, 4 and 6 views for the minimum value approach (a, b, and c respectively). The iso–surfaces of regions with L_p 3, 6, 9, and 12 dB below the peak are presented. The microphone positions are denoted as dots.

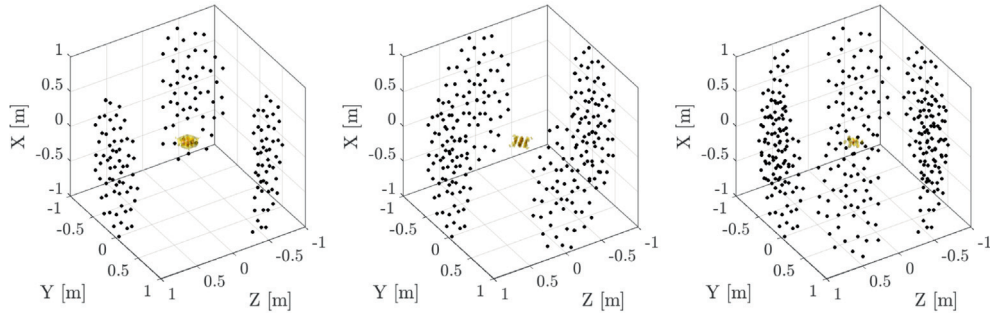

(a) $N_s = 3$ (b) $N_s = 4$ (c) $N_s = 6$

Fig. A.11. 3D source maps for the *Synthetic case III* at 4 kHz using 3, 4 and 6 views for equivalent synchronous measurements (a, b, and c respectively). The iso–surfaces of regions with L_p 3, 6, 9, and 12 dB below the peak are presented. The microphone positions are denoted as dots.

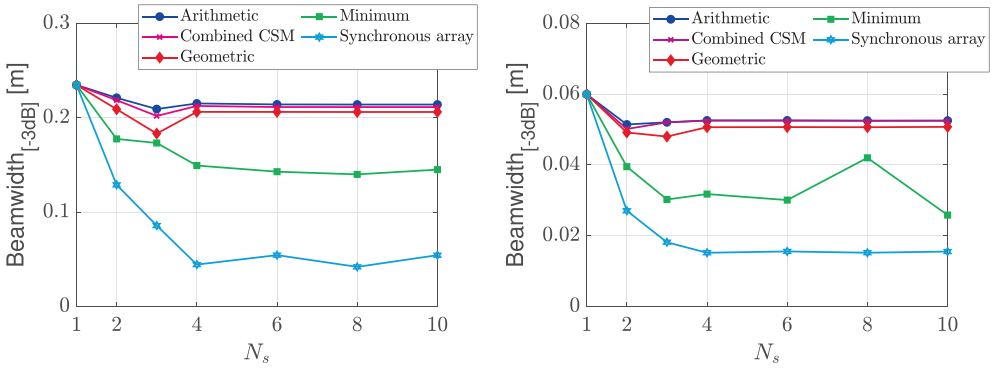

(a) $f = 1$ kHz (b) $f = 4$ kHz

Fig. A.12. Variation of the beamwidth at −3 dB for the different 3D techniques applied to the *Synthetic case III* with the number of asynchronous measurements (N_s) for $f = 1$ kHz (a) and $f = 4$ kHz (b).

array. The additional computational time required by the methods suggested in this manuscript scales as $\propto N_s$, since the computational time required for combining source maps is negligible. The combined CSM approach also presents a $\propto N_s$ scaling provided that a sparse representation is used to create the CSM, avoiding computational time to scale with N_s^2 with the postprocessing of non–existent cross–correlations.

References

[1] Environmental Noise Guidelines for the European Region, Tech. Rep. ISBN 978 92 890 5356 3, World Health Organization. Regional Office for Europe, Copenhagen, Denmark (2018). http://www.euro.who.int/_data/assets/pdf_file/0008/383921/noise-guidelines-eng.pdf?ua=1.

[2] M.J.T. Smith, Aircraft Noise, 1st Edition, Cambridge University Press, 1989, ISBN: 0-521-33186-2. doi:https://doi.org/10.1017/CBO9780511584527. https://www.cambridge.org/core/books/aircraft-noise/7C4059C54DF8EC87C2F34262BC865E36.

[3] Bartels S, Márki F, Müller U. The influence of acoustical and non–acoustical factors on short–term annoyance due to aircraft noise in the field – The COSMA study. Sci Total Environ 2015;538:834–43. https://doi.org/10.1016/j.scitotenv.2015.08.064.

[4] R. Merino-Martinez, L. Bertsch, M. Snellen, D.G. Simons, Analysis of landing gear noise during approach, in: 22nd AIAA/CEAS Aeroacoustics Conference, May 30 – June 1 2016, Lyon, France, 2016, AIAA paper 2016–2769. doi:10.2514/6.2016-2769. http://arc.aiaa.org/doi/pdf/10.2514/6.2016-2769.

[5] Wagner S, Bareiß R, Guidati G. Wind turbine noise. first Ed. Springer; 1996, ISBN 978-3-642-88712-3. https://www.springer.com/gp/book/9783642887123.

[6] Oerlemans S, Sijtsma P, Méndez López B. Location and quantification of noise sources on a wind turbine. J Sound Vib 2007;299:869–83.

[7] Barsikow B, King III WF, Pfizenmaier E. Wheel/rail noise generated by a high-speed train investigated with a line array of microphones. J Sound Vib 1987;118:99–122. https://doi.org/10.1016/0022-460X(87)90257-4.

[8] U. Michel, B. Barsikow, Localisation of sound sources on moving vehicles with microphone arrays. In: Proceedings of EuroNoise 2003, May 19–21 2003, Naples, Italy, no. paper ID 537, 2003. https://www.researchgate.net/publication/263887686_Localisation_of_sound_sources_on_moving_vehicles_with_microphone_ arrays.

[9] Fonseca WD, Gerges SNY, Dougherty RP. Pass–by noise measurements using beamforming technique. In: Inter–Noise 2008, Shangai, China.

[10] P. Sijtsma, S. Oerlemans, H. Holthusen, Location of rotating sources by phased array measurements, in: 7th AIAA/CEAS Aeroacoustics Conference, May 28–30, 2001, Maastricht, the Netherlands, 2001, AIAA paper 2001–2167. doi:10.2514/6.2001-2167. https://arc.aiaa.org/doi/pdf/10.2514/6.2001-2167.

[11] Herold G, Sarradj E. Microphone array method for the characterization of rotating sound sources in axial fans. Noise Control Eng J 2015;63(6):546–51. https://www-docs.b-tu.de/fg-akustik/public/veroeffentlichungen/herold_rotating_ncej2015.pdf.

[12] L.C. Caldas, P.C. Greco, C.C.J. Pagani, L.A. Baccalá, Comparison of different techniques for rotating beamforming at the university of São Paulo fan rig test facility, in: 6th Berlin Beamforming Conference, February 29 – March 1 2016, Berlin, Germany, GFaI, e.V., Berlin, 2016, BeBeC–2016–D14. http://www.bebec.eu/Downloads/BeBeC2016/Papers/BeBeC-2016-D14.pdf.

[13] ICAO Annex 16 Chapter 3. Environmental protection., Tech. rep., International Civil Aviation Organization (ICAO), Montreal, Canada (2005).

[14] Mueller T. Aeroacoustic measurements. Berlin, Germany: Springer Science & Business Media; 2002, ISBN 978-3-642-07514-8. https://books.google.com/books?hl=en&lr=&id=MU6WLXFJLWgC&pgis=1.

[15] P. Sijtsma, Phased array beamforming applied to wind tunnel and fly–over tests, Tech. Rep. NLR-TP-2010-549, National Aerospace Laboratory (NLR), Anthony Fokkerweg 2, 1059 CM Amsterdam, P.O. Box 90502, 1006 BM Amsterdam, The Netherlands (December 2010). https://reports.nlr.nl/xmlui/bitstream/handle/10921/192/TP-2010-549.pdf?sequence=1..

[16] Merino-Martinez R, Sijtsma P, Snellen M, Ahlefeldt T, Antoni J, Bahr CJ, Blacodon D, Ernst D, Finez A, Funke S, Geyer TF, Haxter S, Herold G, Huang X, Humphreys WM, Leclère Q, Malgoezar A, Michel U, Padois T, Pereira A, Picard C, Sarradj E, Siller H, Simons DG, Spehr C. A review of acoustic imaging methods using phased microphone arrays (part of the Aircraft Noise Generation and Assessment special issue). CEAS Aeronaut J 2019;10(1):197–230. https://doi.org/10.1007/s13272-019-00383-4. https://rdcu.be/brsL2.

[17] Chiariotti P, Martarelli M, Castellini P. Acoustic beamforming for noise source localization – Reviews, methodology and applications. Mech Syst Signal Process 2019;120:422–48. https://doi.org/10.1016/j.ymssp.2018.09.019.

[18] van Veen BD, Buckley KM. Beamforming: A Versatile Approach to Spatial Filtering. IEEE ASSP Magazine 1988;5(2):4–24. https://doi.org/10.2514/1.C033020. http://ieeexplore.ieee.org/document/665/.

[19] Johnson DH, Dudgeon DE. Array signal processing, concepts and techniques. Englewood Cliffs: P T R Prentice Hall; 1993, ISBN 978-0130485137. https://books.google.nl/books/about/Array_Signal_Processing.html?id=v_NSAAAAMAAJ&redir_esc=y.

[20] R. Merino-Martinez, Microphone arrays for imaging of aerospace noise sources, Ph.D. thesis, Delft University of Technology, ISBN: 978-94-028-1301-2 (2018). doi:10.4233/uuid:a3231ea9-1380-44f4-9a93-dbbd9a26f1d6. https://repository.tudelft.nl/islandora/object/uuid:a3231ea9-1380-44f4-9a93-dbbd9a26f1d6?collection=research.

[21] J. Benesty, J. Chen, H. Yiteng, Microphone array signal processing, Springer Science & Business Media, 2008, ISBN: 978-3-540-78611-5. doi:10.1007/978-3-540-78612-2.

[22] F.R.S. Lord Rayleigh, XXXI. Investigations in Optics with special reference to the Spectroscope, The London, Edinburgh and Dublin Philos Mag J Sci 1879:8(49):261–274. doi:10.1080/14786447908639684. doi: 10.1080/14786447908639684.

[23] E. Sarradj, A generic approach to synthesize optimal array microphone arrangements, in: 6th Berlin Beamforming Conference, February 29 – March 1 2016, Berlin, Germany, GFaI, e.V., Berlin, 2016, BeBeC–2016–S4. http://www.bebec.eu/Downloads/BeBeC2016/Papers/BeBeC-2016-S4.pdf.

[24] A.M.N. Malgoezar, M. Snellen, P. Sijtsma, D.G. Simons, Improving beamforming by optimization of acoustic array microphone positions, in: 6th Berlin Beamforming Conference, February 29– March 1 2016, Berlin, Germany, 2016. http://www.bebec.eu/Downloads/BeBeC2016/Papers/BeBeC-2016-S5.pdf.

[25] Luesutthiviboon S, Malgoezar AMN, Merino-Martinez R, Snellen M, Sijtsma P, Simons DG. Enhanced HR-CLEAN-SC for resolving multiple closely spaced sound sources. Int J Aeroacoust 2019;18(4–5):392–413. https://doi.org/10.1177/1475472X19852938.

[26] Arcondoulis E, Liu Y, Xu P, Chen N. Application of the adaptive array reduction method for offset acoustic source localisation. J Sound Vib 2020;478:1–22. https://doi.org/10.1016/j.jsv.2020.115358.

[27] S. Oerlemans, Detection of aeroacoustic sound sources on aircraft and wind turbines, Ph.D. thesis, University of Twente, Enschede, the Netherlands (2009). http://doc.utwente.nl/67363/1/thesis_S_Oerlemans.pdf.

[28] Zhou Y, Valeau V, Marchal J, Ollivier F, Marchiano R. Three-Dimensional identification of flow induced noise sources with a tunnel–shaped array of MEMS microphones. J Sound Vib 2020;482:1–20. https://doi.org/10.1016/j.jsv.2020.115459.

[29] T.F. Brooks, W.M. Humphreys, Three-dimensional application of DAMAS methodology for aeroacoustic noise source definition. In: 11th AIAA/CEAS aeroacoustics conference, May 23–25 2005, Monterey, California, USA, 2005, AIAA paper 2005–2960. doi:10.2514/6.2005-2960. http://arc.aiaa.org/doi/pdf/10.2514/6.2005-2960.

[30] Evans D, Hartmann M, Delfs J. Beamforming for point force surface sources in numerical data. J Sound Vib 2019;458:303–19. https://doi.org/10.1016/j.jsv.2019.05.030.

[31] P.A. Ravetta, M.R. Khorrami, B. König, E. Fares, Analysis of simulated and experimental noise sources of the boeing 777 main gear model via CLEAN in 3D, in: 24th AIAA/CEAS Aeroacoustics Conference, June 25–29 2018, Atlanta, Georgia, USA, 2018, AIAA paper 2018–3470. doi:10.2514/6.2018-3470. http://arc.aiaa.org/doi/pdf/10.2514/6.2018-3470.

[32] M. Tuinstra, M. van der Meulen, Acoustic location by tomographic reconstruction, in: 25th AIAA/CEAS Aeroacoustics Conference, May 20–24 2019, Delft, The Netherlands, 2019, AIAA paper 2019–2409. doi:10.2514/6.2019-2409. http://arc.aiaa.org/doi/pdf/10.2514/6.2019-2409.

[33] Zamponi R, Chiariotti P, Battista G, Schram C, Castellini P. 3D generalized inverse beamforming in wind tunnel aeroacoustic testing: application to a counter rotating open rotor aircraft model. Appl Acoust 2020;163(107229):1–11. https://doi.org/10.1016/j.apacoust.2020.107229.

[34] Merino-Martinez R, Kennedy J, Bennett GJ. Aerosp Sci Technol 2021;113(106705):1–20. https://doi.org/10.1016/j.ast.2021.106705. https://www.sciencedirect.com/science/article/pii/S1270963821002157?via.

[35] Geyer T, Sarradj E, Giesler J. Application of a beamforming technique to the measurement of airfoil leading edge noise. Adv Acoust Vib 2012;2012(905461):1–16. https://doi.org/10.1155/2012/905461.

[36] J. Ocker, S. Tilgner, The porsche wind tunnel microphone array system. In: Aachen acoustics colloquium, November 23 – 25, 2015, Aachen, Germany, 2015, pp. 135–151. https://www.polytec.com/fileadmin/d/The_Acoustic_Camera/AAC2015_Proceedings_Porsche_Array.pdf.

[37] D. Döbler, J. Ocker, C. Puhle, On 3D–beamforming in the wind tunnel. In: 6th Berlin beamforming conference, February 29 – March 1 2016, Berlin, Germany, GFaI, e.V., Berlin, 2016, BeBeC–2016–S10. http://www.bebec.eu/Downloads/BeBeC2016/Papers/BeBeC-2016-S10.pdf..

[38] R.P. Dougherty, Jet noise beamforming with several techniques. In: 3th Berlin beamforming conference, February 24–25 2010, Berlin, Germany, GFaI, e.V., Berlin, 2010. http://bebec.eu/Downloads/BeBeC2010/Papers/BeBeC-2010-17.pdf.

[39] Sarradj E. Three-dimensional acoustic source mapping with different beamforming steering vector formulations. Adv Acoust Vib 2012;2012(292695):1–12. https://doi.org/10.1155/2012/292695.

[40] Porteous R, Prime Z, Doolan CJ, Moreau DJ. Three–dimensional beamforming of dipolar aeroacoustic sources. J Sound Vib 2015;355:117–34. https://doi.org/10.1016/j.jsv.2015.06.030. DOI: 10.1016/j.jsv.2015.06.030.

[41] Malgoezar AMN, Snellen M, Merino-Martinez R, Simons DG, Sijtsma P. On the use of global optimization methods for acoustic source mapping. J Acoust Soc Am 2017;141(1):453–65. https://doi.org/10.1121/1.4973915.

[42] G. Battista, P. Chiariotti, M. Martarelli, P. Castellini, Inverse methods in aeroacoustic three–dimensional volumetric noise source localization and quantification. J Sound Vib 2020;473(20200):1–26. doi:10.1016/j.jsv.2020.115208.

[43] Hileman J, Thurow B, Samimy M. Development and evaluation of a 3–D microphone array to locate individual acoustic sources in a high–speed jet. J Sound Vib 2004;276:649–69. https://doi.org/10.1016/j.jsv.2003.08.022.

[44] D. Ernst, C. Spehr, Three-dimensional microphone array for wind tunnel application. In: 46th international congress and exposition of noise control engineering, 27–30 August, 2017, Hong Kong, International Institute of Noise Control Engineering (I-INCE), 2017.

[45] J. Chambon, T. Le Magueresse, O. Minck, J. Antoni, Three–dimensional beamforming for wind tunnel applications using ESM based transfer functions. In 8th Berlin beamforming conference, March 2–3 2020, Berlin, Germany, GFaI, e.V., Berlin, 2020, BeBeC–2020–S09. http://www.bebec.eu/Downloads/BeBeC2020/Papers/BeBeC-2020-S09.pdf.

[46] T. Padois, O. Robin, A. Berry, 3D source localization in a closed wind–tunnel using microphone arrays. In 19th AIAA/CEAS aeroacoustics conference, May 27–29 2013, Berlin, Germany, 2013, AIAA paper 2013–2213. doi:10.2514/6.2013-2213. http://arc.aiaa.org/doi/pdf/10.2514/6.2013-2213.

[47] Cigada A, Lurati M, Ripamonti F, Vanali M. Moving microphone arrays to reduce spatial aliasing in the beamforming technique: Theoretical background and numerical investigation. J Acoust Soc Am 2008;124(6):3648–58. https://doi.org/10.1121/1.2998778.

[48] Castellini P, Martarelli M. Acoustic beamforming: Analysis of uncertainty and metrological performances. Mech Syst Signal Process 2008;22(3):672–92. https://doi.org/10.1016/j.ymssp.2007.09.017.

[49] G. Heilmann, D. Döbler, A. Meyer, S. Barre, Dynamic beamforming using moving phased arrays with integrated 3D scanners. In: 46th international congress and exposition of noise control engineering, 27–30 August, 2017, Hong Kong, International Institute of Noise Control Engineering (I-INCE), 2017.

[50] L.K. Wächter, J. Ocker, D. Döbler, C. Puhle, G. Herold, Investigations on beamforming in the wind tunnel using multiple microphone array measurements. In: 7th Berlin beamforming conference, March 5–6 2018,

Berlin, Germany, GFaI, e.V., Berlin, 2018, BeBeC–2018–S09. http://www.bebec.eu/Downloads/BeBeC2018/Papers/BeBeC-2018-S09.pdf.
[51] L. Yu, W. Jiang, J. Antoni, Q. Leclère, H. Wu, Acoustic beamforming by non-synchronous microphone array measurements. In: 7th Berlin beamforming conference, March 5–6 2018, Berlin, Germany, GFaI, e.V., Berlin, 2018, BeBeC–2018–S10. http://www.bebec.eu/Downloads/BeBeC2018/Papers/BeBeC-2018-S10.pdf.
[52] Chu N, Ning Y, Yu L, Huang Q, Wu D. A high-resolution and low-frequency acoustic beamforming based on bayesian inference and non-synchronous measurements. IEEE Access 2020;8:82500–13. https://doi.org/10.1109/ACCESS.2020.2991606. https://ieeexplore.ieee.org/document/9082683.
[53] Ning F, Song J, Hu J, Wei J. Sound source localization of non–synchronous measurements beamforming with block Hermitian matrix completion. Mech Syst Signal Process 2020;147(107118):1–14. https://doi.org/10.1016/j.ymssp.2020.107118.
[54] D.G. Simons, M. Snellen, R. Merino-Martinez, A.M.N. Malgoezar. In: 46th international congress and exposition of noise control engineering, 27–30 August, 2017, Hong Kong, International Institute of Noise Control Engineering (I-INCE), 2017. https://repository.tudelft.nl/islandora/object/uuid%3Afc38f80c-ed6b-4b3f-b664-bb47b96b5be1.
[55] M.C. Remillieux, E.D. Crede, H.E. Camargo, R.A. Burdisso, D.W.J., M. Rasnick, P. van Seeters, A. Chou, Calibration and demonstration of the new virginia tech anechoic wind tunnel. In: 14th AIAA/CEAS aeroacoustics conference 29th AIAA Aeroacoustics Conference), May 5–7, 2008, Vancouver, British Columbia, Canada, 2008, AIAA paper 2008–2911. doi:10.2514/6.2008-2911. http://arc.aiaa.org/doi/pdf/10.2514/6.2008-2911.
[56] H. Holthusen, A. Bergmann, P. Sijtsma, Investigations and measures to improve the acoustic characteristics of the german-dutch wind tunnel DNW–LLF. In: 18th AIAA/CEAS Aeroacoustics Conference, 4–6 June 2012, Colorado Springs, USA, 2012, AIAA paper 2012–2176. doi:10.2514/6.2012-2276. http://arc.aiaa.org/doi/pdf/10.2514/6.2012-2176.
[57] P. Sijtsma, R. Merino-Martinez, A.M.N. Malgoezar, M. Snellen, High-resolution CLEAN-SC: theory and experimental validation. Int J Aeroacoust 2017;16(4–5):274–298, SAGE Publications Ltd., London, United Kingdom. doi:10.1177/1475472X17713034. http://journals.sagepub.com/doi/10.1177/1475472X17713034.
[58] C.J. Bahr, W.M. Humphreys, D. Ernst, T. Ahlefeldt, C. Spehr, A. Pereira, Q. Leclère, C. Picard, R. Porteus, D.J. Moreau, J. Fischer, C.J. Doolan, A comparison of microphone phased array methods applied to the study of airframe noise in wind tunnel testing. In: 23th AIAA/CEAS aeroacoustics conference, June 5–9 2017, Denver, CO, USA, 2017, AIAA paper 2017–3718. doi:10.2514/6.2017-3718. http://arc.aiaa.org/doi/pdf/10.2514/6.2017-3718.
[59] J. Fischer, C.J. Doolan, The evaluation of methods for improving beamforming maps in noisy environment. In: 7th Berlin beamforming conference, March 5–6 2018, Berlin, Germany, GFaI, e.V., Berlin, 2018, BeBeC–2018–D13. http://www.bebec.eu/Downloads/BeBeC2018/Papers/BeBeC-2018-D13.pdf.
[60] R. Merino-Martinez, M.P.J. Sanders, L.C. Caldas, F. Avallone, D. Ragni, L.D. de Santana, M. Snellen, D.G. Simons, Comparison between analog and digital microphone phased arrays for aeroacoustic measurements, in: 24th AIAA/CEAS aeroacoustics conference, June 25–29 2018, Atlanta, Georgia, USA, 2018, AIAA paper 2018–2809. doi:10.2514/6.2018-2809. http://arc.aiaa.org/doi/pdf/10.2514/6.2018-2809.
[61] Merino-Martinez R, Neri E, Snellen M, Kennedy J, Simons DG, Bennett GJ. Multi–approach study of nose landing gear noise. J Aircr 2020;57(3):517–33. https://doi.org/10.2514/1.C035655.
[62] R. Merino-Martinez, A. Rubio Carpio, L.T. Lima Pereira, S. van Herk, F. Avallone, M. Kotsonis, D. Ragni, Aeroacoustic design and characterization of the 3D–printed, open–jet, anechoic wind tunnel of delft university of technology. Appl Acoust 2020;170(107504):1–16. doi:10.1016/j.apacoust.2020.107504. doi:10.1016/j.apacoust.2020.107504.
[63] E.J.G. Arcondoulis, Y. Liu, P. Xu, N. Chen, An array pairing method for localizing distributed sources by acoustic beamforming. J Acoust Soc Ame – Expr Lett 2020;147(1):E7–E12. doi:10.1121/10.0000496. doi: 10.1121/10.0000496.
[64] E. Sarradj, G. Herold, P. Sijtsma, R. Merino-Martinez, A.M.N. Malgoezar, M. Snellen, T.F. Geyer, C.J. Bahr, R. Porteous, D.J. Moreau, C.J. Doolan, A microphone array method benchmarking exercise using synthesized input data. In: 23th AIAA/CEAS aeroacoustics conference, June 5–9 2017, Denver, CO, USA, 2017, AIAA paper 2017–3719. doi:10.2514/6.2017-3719. http://arc.aiaa.org/doi/pdf/10.2514/6.2017-3719.
[65] Merino-Martinez R, Sijtsma P, Rubio Carpio A, Zamponi R, Luesutthiviboon S, Malgoezar AMN, Snellen M, Schram C, Simons DG. Integration methods for distributed sound sources. Int J Aeroacoust 2019;18(4–5):444–69. https://doi.org/10.1177/1475472X19852945.
[66] R. Merino-Martinez, S. Luesutthiviboon, R. Zamponi, A. Rubio Carpio, D. Ragni, P. Sijtsma, M. Snellen, C. Schram, Assessment of the accuracy of microphone array methods for aeroacoustic measurements. J Sound Vib 2020;470(115176):1–24. doi:10.1016/j.jsv.2020.115176. doi: 10.1016/j.jsv.2020.115176.
[67] Brooks TF, Humphreys WM. A Deconvolution Approach for the Mapping of Acoustic Sources (DAMAS) determined from phased microphone arrays. J Sound Vib 2006;294(4–5):856–79. https://doi.org/10.1016/j.jsv.2005.12.046.
[68] Liu Y, Quayle AR, Dowling AP, Sijtsma P. Beamforming correction for dipole measurement using two–dimensional microphone arrays. J Acoust Soc Am 2008;124(1):182–91. https://doi.org/10.1121/1.2931950.
[69] Merino-Martinez R, Snellen M, Simons DG. Functional beamforming applied to imaging of flyover noise on landing aircraft. J Aircr 2016;53(6):1830–43. https://doi.org/10.2514/1.C033691. http://arc.aiaa.org/doi/abs/10.2514/1.C033691.
[70] P. Sijtsma, Fast calculation of microphone array steering vectors with shear flow. In: 7th Berlin beamforming conference, March 5–6 2018, Berlin, Germany, GFaI, e.V., Berlin, 2018, BeBeC–2018–S03. http://www.bebec.eu/Downloads/BeBeC2018/Papers/BeBeC-2018-S03.pdf.
[71] Castellini P, Sassaroli A. Acoustic source localization in a reverberant environment by average beamforming. Mech Syst Signal Process 2010;24:796–808. https://doi.org/10.1016/j.ymssp.2009.10.021.
[72] P. Sijtsma, CLEAN based on spatial source coherence, International Journal of Aeroacoustics 6 (4) (2007) 357–374, SAGE Publications Ltd., London, United Kingdom. doi:10.1260/147547207783359459. doi: 10.1260/147547207783359459.
[73] R.P. Dougherty, Functional beamforming. In: 5th Berlin beamforming conference, February 19–20 2014, Berlin, Germany, GFaI, e.V., Berlin, 2014, BeBeC-2014-01. http://bebec.eu/Downloads/BeBeC2014/Papers/BeBeC-2014-01.pdf.
[74] Welch PD. The use of fast fourier transform for the estimation of power spectra: a method based on time averaging over short, modified periodograms. IEEE Trans Audio Electroacoust 1967;AU–15(2):70–3. https://doi.org/10.1109/TAU.1967.1161901. http://ieeexplore.ieee.org/stamp/stamp.jsp?arnumber=1161901.
[75] Vieira A, Snellen M, Malgoezar AMN, Merino-Martinez R, Simons DG. Analysis of shielding of propeller noise using beamforming and predictions. J Acoust Soc Am 2019;146(2):1085–98. https://doi.org/10.1121/1.5121398.
[76] Flamex basic – acoustic absorbing foam, https://www.merford.com/media/202626/flamex-basic.pdf, accessed in March 2017. https://www.merford.com/media/202626/flamex-basic.pdf.
[77] G.R.A.S. Sound & vibration – 40PH CCP free–field array microphone, http://www.gras.dk/products/special-microphone/array-microphones/product/178-40ph, accessed in March 2017. http://www.gras.dk/products/special-microphone/array-microphones/product/178-40ph.
[78] G.R.A.S. Sound & Vibration – AA0028 10 m SMB – BNC cable, https://www.gras.dk/products/cables/product/418-aa0028-extension-cable-for-array-microphones-smb-female-to-bnc, accessed in March 2017. https://www.gras.dk/products/cables/product/418-aa0028-extension-cable-for-array-microphones-smb-female-to-bnc.
[79] G.R.A.S. Sound & vibration – 42AA Pistonphone class 1, https://www.gras.dk/products/calibration-equipment/reference-calibrator/product/255-42aa, accessed in March 2017. https://www.gras.dk/products/calibration-equipment/reference-calibrator/product/255-42aa.
[80] Qsources website, https://www.qsources.be/qindw/, accessed in June 2021..
[81] Lima Pereira LT, Ragni D, Avallone F, Scarano F. Pressure fluctuations from large–scale PIV over a serrated trailing edge. Exp Fluids 2020;61:1–17. https://doi.org/10.1007/s00348-020-2888-x.
[82] C. Arce León, R. Merino-Martinez, D. Ragni, F. Avallone, M. Snellen, Boundary layer characterization and acoustic measurements of flow–aligned trailing edge serrations, Experim Fluids 57 (182) (2016) 1–22. doi:10.1007/s00348-016-2272-z. http://link.springer.com/10.1007/s00348-016-2272-z..
[83] Parrot – Drone Camera 4k HRD ANAFI, https://www.parrot.com/global/drones/anafi, accessed in March 2020. https://www.parrot.com/global/drones/anafi.
[84] Snellen M, Merino-Martinez R, Simons DG. Assessment of noise level variability on landing aircraft using a phased microphone array. J Aircr 2017;54(6):2173–83. https://doi.org/10.2514/1.C033950.
[85] E. Arcondoulis, Y. Liu, P. Xu, Q. Li, R. Wei, Y. Yang, N. Chen, Experimental application of an acoustic beamforming array pairing method using CLEAN–SC. In: AIAA SciTech forum, January 19–21 2021, Virtual Event, 2021, AIAA paper 2021–0214. doi:10.2514/6.2021-0214. http://arc.aiaa.org/doi/pdf/10.2514/6.2021-0214.
[86] Heutschi K, Ott B, Nussbaumer T, Wellig P. Synthesis of real world drone signals based on lab recordings. Acta Acoust 2020;4(24):1–10. https://doi.org/10.1051/aacus/2020023.